JOURNAL OF GEOPHYSICAL RESEARCH: OCEANS, VOL. 118, 6894–6913, doi:10.1002/2013JC008981, 2013

The pathways and properties of the Amazon River Plume in the tropical North Atlantic Ocean

Victoria J. Coles,[1] Maureen T. Brooks,[1] Julia Hopkins,[2] Michael R. Stukel,[1] Patricia L. Yager,[3] and Raleigh R. Hood[1]

Received 3 April 2013; revised 11 November 2013; accepted 13 November 2013; published 17 December 2013.

[1] The Amazon River Plume spreads across the tropical North Atlantic creating a barrier to vertical mixing. Here using a 1/6° HYCOM model and data from three research cruises in May–June 2010, September–October 2011, and July 2012, we investigate the pathways and properties of the plume. Four plume pathways for export of freshwater from the western tropical North Atlantic are identified. These consist of direct and indirect pathways to the northwest, and eastward pathways toward the subtropical gyre and toward Africa in the North Equatorial Counter Current. Because of the seasonality and cooccurrence of these pathways, plume characteristics are highly variable. Two pathways export water to the Caribbean, however the time scales associated with those direct and indirect pathways (3 versus 6+ months) differ, leading to different salinity characteristics of the plume water. Models results show that the Amazon river and tropical precipitation have similar magnitude impact on the observed seasonal cycle of freshwater within the western tropical Atlantic and at the 8°N, 38°W PIRATA mooring. Freshwater associated with the Amazon also influences surface salinity in winter as far as 20W in the model. The mean plume salinity minimum leads maximum discharge, highlighting the importance of currents and advection rather than discharge in maintaining plume properties. Plume pathways are tied to the underlying current structure, with the North Equatorial Counter Current jet preventing direct freshwater transport into the southern hemisphere. The plume influences underlying currents as well, generating vertical current shear that leads to enhanced eddy stirring and mixing in the model simulations.

Citation: Coles, V. J., M. T. Brooks, J. Hopkins, M. R. Stukel, P. L. Yager, and R. R. Hood (2013), The pathways and properties of the Amazon River Plume in the tropical North Atlantic Ocean, *J. Geophys. Res. Oceans*, *118*, 6894–6913, doi:10.1002/2013JC008981.

1. Introduction

[2] The Amazon River main stem stretches 6500 km across South America, draining nearly one third of the continent [*Nittrouer and DeMaster*, 1986], and depositing almost 20% of the global river discharge onto the continental shelf of the equatorial Atlantic Ocean. The magnitude of this freshwater source is unique in the global oceans; the Amazon River discharges as much freshwater as the next 8 largest rivers in the world combined (calculated from *Dai and Trenberth* [2002]). Consequently, the Amazon River serves as an important connection between continental hydrology and the ocean. Typically, river discharge is a small component of the open ocean salinity balance but the Amazon discharge volume is twice the evaporation minus precipitation budget integrated over the region of 0°–10°N, 70°–20°W based on the European Center for Medium-Range Weather Forecasts reanalysis ERA-15 [*Ferry and Reverdin*, 2004]. Thus, the fate of Amazon River water has a large impact on the tropical Atlantic freshwater budget and its variability.

[3] The influence of Amazon water is felt far from the river mouth through enhancement of surface stratification leading to the formation of barrier layers [*Godfrey and Lindstrom*, 1989; *Lukas and Lindstrom*, 1991]. In particular, the western tropical Atlantic barrier layer [*Pailler et al*., 1999] consists of a shallow fresh cap over a deep isothermal pool, which enhances the trapping of solar radiation in the surface layer leading to elevated sea surface temperature [*Ffield*, 2005; *Foltz and McPhaden*, 2009]. This increase in surface temperature has implications for hurricane intensification [*Vizy and Cook*, 2010; *Grodsky et al*., 2012]. Furthermore, improved model representation of barrier layers and surface temperature has been shown to lead to improved precipitation fields in coupled ocean atmosphere models [*Balaguru et al*., 2012]. Thus, the Amazon River Plume is thought to contribute to the dynamics

[1]University of Maryland Center for Environmental Science, Horn Point Laboratory, Cambridge, Maryland, USA.
[2]Department of Applied Ocean Physics and Engineering, Massachusetts Institute of Technology/Woods Hole Oceanographic Institution Joint Program in Oceanography, Woods Hole, Massachusetts, USA.
[3]Department of Marine Science, University of Georgia, Athens, Georgia, USA.

Corresponding author: V. J. Coles, University of Maryland Center for Environmental Science, Horn Point Laboratory, PO Box 775, Cambridge, MD 21613, USA. (vcoles@umces.edu)

©2013. American Geophysical Union. All Rights Reserved.
2169-9275/13/10.1002/2013JC008981

of ocean atmosphere interaction and climate in the western tropical North Atlantic.

[4] In addition to the physical climate impacts of the Amazon River on the region, the river also injects terrestrially derived sediments, nutrients, and colored as well as transparent dissolved organic matter (CDOM, DOM) which can be traced thousands of kilometers from the Amazon River mouth [*Hu et al*., 2004]. Biological community structure is strongly influenced by these dissolved organic matter and nutrient inputs as well as by the plume's role in stratifying the upper ocean [*Stukel et al*., 2013]. This has been shown to lead to globally significant uptake of atmospheric carbon dioxide in the river plume [*Cooley et al*., 2007; *Subramaniam et al*., 2008].

[5] Because the Amazon discharges at the equator and on the western boundary of the ocean, its waters are entrained in energetic boundary currents associated with the North Brazil Current (NBC), North Equatorial Counter Current (NECC), and coastal Guyana Current (GC) [*Richardson and Reverdin*, 1987]. Strong seasonal variations in these currents occur in response to the annual migration of the atmospheric Intertropical Convergence Zone (ITCZ) between its southern position in winter, and its northern position in summer. This leads to northward transport of Amazon water in winter, and eastward transport of Amazon water in the NECC in spring through fall [*Müller-Karger et al*., 1988, 1989, 1995; *Garzoli*, 1992; *Lentz*, 1995; *Fratantoni and Glickson*, 2002; *Hellweger and Gordon*, 2002; *Hu et al*., 2004]. The northward transport of Amazon water into the Caribbean is debated, with some investigations concluding persistent northward flow throughout the year [*Schott and Böning*, 1991; *Lentz*, 1995; *Hu et al*., 2004] and others suggesting the northward pathway is interrupted in summer and fall [*Philander and Pacanowski*, 1986; *Richardson and Reverdin*, 1987; *Wilson et al*., 1994].

[6] Relating Amazon discharge to plume area is challenging due to the strong seasonality of the current structures. Studies find interesting discrepancies between the phasing of river discharge, satellite derived plume area estimates based on CDOM and salinity, and surface salinity and CDOM concentrations themselves [*Hu et al*., 2004; *Salisbury et al*., 2011] suggesting that plume area may not be a straightforward proxy for plume or freshwater volume. Thus, a better understanding of the plume flow and dissipation is needed to relate river discharge to tropical Atlantic surface salinity fields. Given recent advances in remote sensing of surface salinity coupled with evidence for freshening in the central tropical North Atlantic over decadal and 50 year time scales [*Grodsky et al*., 2006; *Durack and Wijffels*, 2010] further study of the transport of riverine freshwater and its relationship to the seasonal migration of the ITCZ and its associated precipitation is warranted.

[7] In this study, we combine historical observations, three recent field campaigns associated with the Amazon Influences on the Atlantic: Carbon Export from Nitrogen Fixation by Diatom Symbiosis (ANACONDAS) project, and a numerical model in order to investigate Amazon River water in the tropical Atlantic Ocean. The aims are to better understand the pathways of the plume, and the competing influences of precipitation and river flow in driving seasonal salinity variability in the tropical Atlantic. We also investigate the thickness, age and salinity properties of the plume, and the seasonal variations in plume export from the region including persistence of northward river flow into the Caribbean. The relationship between the river plume and upper ocean currents is investigated, and feedback of the plume on surface currents is described.

2. Methods

2.1. Model Description

[8] A Mercator projection 1/6° (18.5–14.2 km resolution in longitude) Hybrid Coordinate Ocean Model (HYCOM) ocean simulation is employed to investigate the seasonal cycle and fate of the Amazon River plume. This spatial grid is sufficient to resolve the first baroclinic Rossby radius of deformation in the tropics (∼60–230 km) [*Chelton et al*., 1998] in the tropical region, but is not highly resolved enough to ensure coastal dynamics are captured. Our efforts therefore, like previous studies at 1/3° or coarser resolution [e.g., *Masson and Delecluse*, 2001; *Ferry and Reverdin*, 2004; *Cotrim da Cunha et al*., 2007; *Balaguru et al*., 2012], focus on plume processes at the shelf break and open ocean. Tides, which have been shown to be important in mixing the plume on the shallow shelf [*Beardsley et al*., 1995; *Lentz and Limeburner*, 1995; *Nikiema et al*., 2007], are neglected. *Nikiema et al*. [2007] show in a high resolution coastal model study, that the introduction of tides accelerates cross shelf plume export of plume water, thus the model is likely to slightly underestimate the rate at which the river water is exported to the shelf break.

[9] HYCOM is a hybrid coordinate model [*Bleck*, 2002; *Chassignet et al*., 2003] that combines pressure, density, and terrain following vertical coordinates depending on the depth and density of the model ocean. It includes realistic bottom topography and coastline geometry based on a modified version of the 1/30° NRL DBDB2 topography (available at http://www7320.nrlssc.navy.mil/DBDB2_WWW). Based on the results of *Schiller and Kourafalou* [2010], we resolve the base of the river plume in isobaric (depth) coordinates to ensure sufficient layer structure to simulate entrainment processes. This is particularly critical in the western Atlantic warm pool region, where subplume density variability is very low, so isopycnal model layers become very thick and little vertical resolution is retained. The model includes 11 isobaric layers in the upper 50 m, ranging from 2 to 8 m in thickness. These fixed layers transition gradually to isopycnal layers in the model ocean interior leading to a total of 28 model layers. K-profile parameterization [*Large et al*., 1994] is utilized for the vertical mixing scheme [*Halliwell*, 2004].

[10] The model domain extends from 40°N to 15°S and 100°W to 15°E including the Caribbean and Gulf of Mexico, with 2° wide sponge layers at the northern and southern boundaries, that are relaxed to World Ocean Atlas 2009 [*Antonov et al*., 2010; *Locarnini et al*., 2010] monthly temperature and salinity climatologies. Surface forcing is prescribed based on the 1.125°, European Centre for Medium-Range Weather Forecasts (ECMWF) 40 year reanalysis over the years 1979–1998 [*Uppala et al*., 2005], adapted following *Kara et al*. [2009] with 6 hourly forcing intervals. A 180 day salinity restoring condition (to avoid restoring the seasonal cycle) is applied at the surface to the

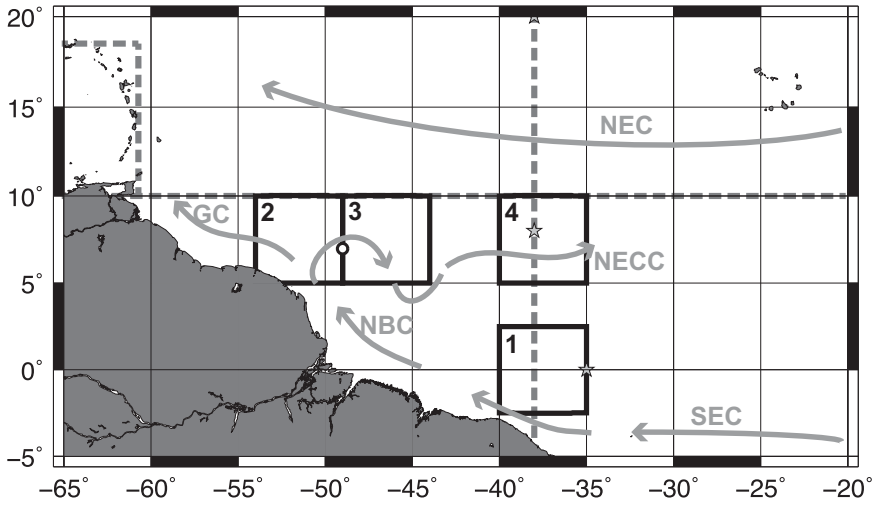

Figure 1. Map of numbered boxes (black lines) showing regional boundaries used in Figure 3, boundaries used for the float trajectory analysis (gray dashed lines) as well as locations of PIRATA moorings used in this study (stars), location of frontal station (circle) and mean currents (gray arrows) following *Bourlès et al*. [1999b].

region where surface salinity is >10, and the relaxation is capped at a 1 salinity unit difference to minimize relaxation influences over the plume region. This relaxation was required to balance a slight model drift to lower basin average surface salinity, however the plume dynamics are very similar to a comparable simulation without the weak salinity restoration. We also use a 17 term empirical equation of state designed to better represent water density at lower salinities in order to more accurately characterize near field plume dynamics (A. Wallcraft, personal communication, 2011).

[11] Climatological discharge from a total of 315 individual rivers from the RIVDIS database [*Vorosmarty et al*., 1998] is included in the model as a climatological mass flux of precipitation that is uniformly mixed over the upper 15 m in the model. This data set differs slightly from the climatological result of summing the discharge from the Brazilian Operador Nacional do Sistema Eletrico stations for: River Amazonas at Óbidos; River Curua at Boca do Inferno; River Tapajós at Jatobá; River Curua-Una at Barragem—Jusante; River Maicuru at Arapari; River Paru de Este at Fazenda Paquira; River Xingu at Altamira; River Jari at São Francisco and River Tocantins at Tucuruí (http://www.ons.org.br/operacao/vazoes_naturais.aspx), however the average monthly climatology discharge difference is <2%, with the greatest difference <4%. This use of climatological data is consistent with the results of *Masson and Delecluse* [2001], who found the Amazon plume spread to be controlled by ocean dynamics rather than discharge volume. The five largest rivers in the model (Amazon, Zaire, Orinoco, Mississippi, Tocantins) are spread over more than one grid cell to distribute river discharge over a wider area. In particular, the Amazon and Tocantins Rivers which both discharge near the equator and whose combined influence we refer to as the Amazon Plume, are divided between 8 grid cells in the model (48.2°W, 0.75°S to 50.0°W, 0.85°N) consistent with the breadth of the Amazon and Tocantins mouth complex (2.4°).

[12] The model is run from 1979 to 1998 (20 years) to spin up current and density fields, then the sequence is repeated and analyzed. Our focus in this paper is on the mean pathways, however pathways that emerge from a climatological simulation may not in fact be representative of any single year. Thus, representative years (1979, 1985, 1991, 1992) that span low to high NECC transport and seasonal variance in transport (see Table 2) are chosen to illustrate the plume pathways, and the interannual variability in pathways and transports is left for a further effort. Surface drifters initialized at 10 day intervals are advected at hourly time steps online in the numerical model [*Halliwell et al*., 2003; *Poje et al*., 2010]. The drifters are initialized at randomized locations within a 0.5° wide band across the river mouth (49.421°W, 1.702°N to 47.257°W, 0.498°S) and integrated forward for 1 year following initialization. Of the 7300 initialized, 6291 drifters did not run aground.

2.2. Data Description

[13] Data sets used here include surface drifters, historical profiles of temperature and salinity, and Prediction and Research Moored Array in the Atlantic (PIRATA) buoy data [*Servain et al*., 1998; *Bourlès et al*., 2008] (Figure 1). Tropical Atlantic surface drifter positions interpolated to 6 hourly intervals (1979–2011) were acquired from the Global Drifter Program Drifter Data Assembly Center following their processing [*Hansen and Poulain*, 1996]. Only drogued drifters that entered a small box around the mouth of the Amazon River (1°S–3°N, 50°W–44°W between 1997 and 2011) are analyzed. The observed drifters do not have uniform initial spatial and temporal distributions, and only 72 of 119 drifters did not run aground near the river mouth, thus the comparison between model and observed drifters is necessarily qualitative. Historical vertical profiles of salinity were obtained from the National Oceanographic Data Center World Ocean Database [*Boyer et al*., 2009]. Surface and 40 m salinity time series from the PIRATA array are also used for model validation.

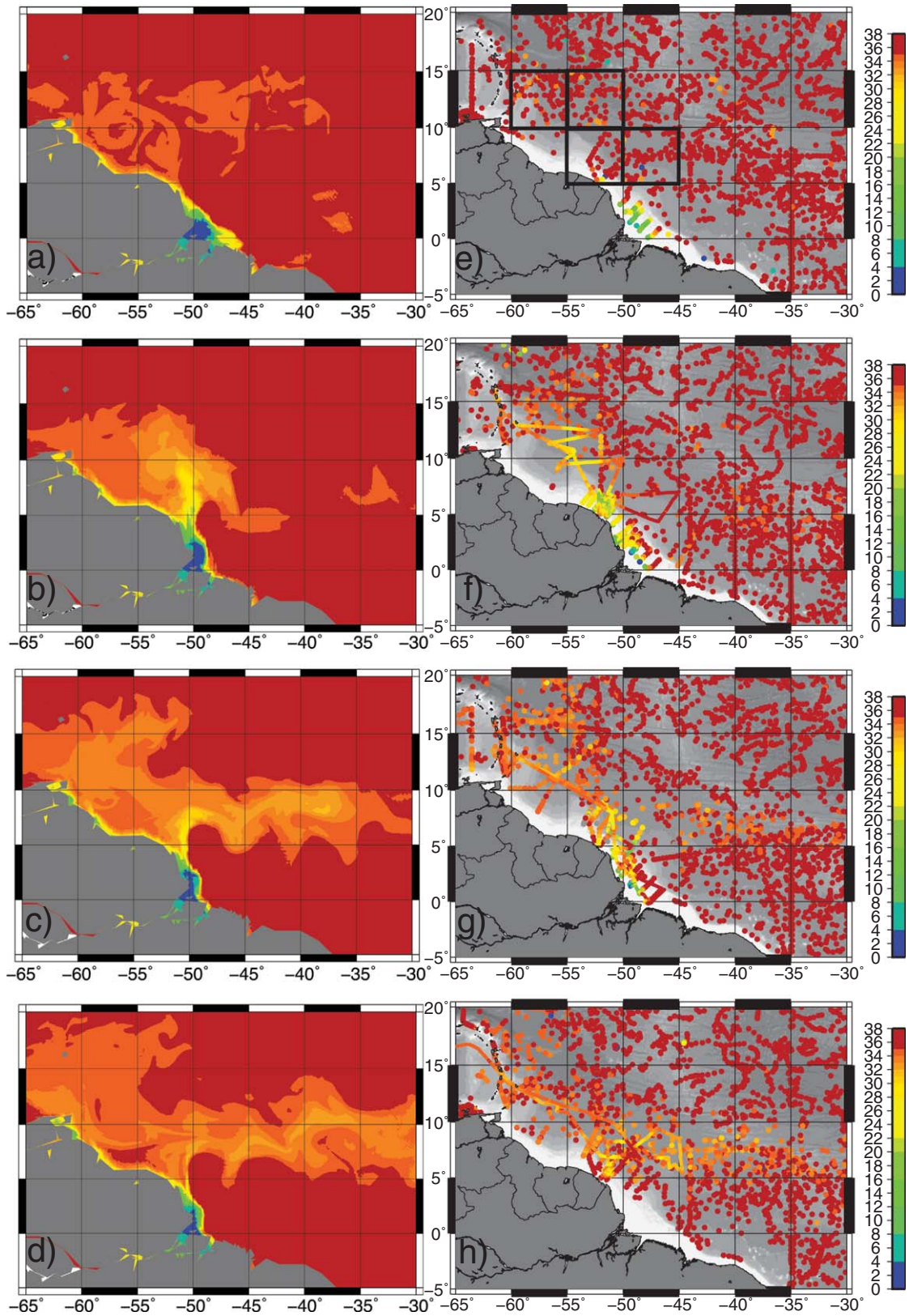

Figure 2. Surface salinity. (a) Model 30 January 1992, (b) Model 30 May 1992, (c) Model 30 July 1992, (d) Model 30 September 1992, (e)World Ocean Database (WOD) January–February, (f)WOD, May–June with ANACONDAS May–June 2010 underway salinity overlain in smaller circles, (g) WOD July–August with ANACONDAS July–August 2012 underway salinity, (h) WOD September–October with ANACONDAS September–October 2011underway salinity. Boxes used in Table 1 are shown in panel e.

Table 1. Average Salinity Within Regions for Model and Observations[a]

Box	Data set	Winter (Jan–Feb)	Spring (May–Jun)	Summer (Jul–Aug)	Fall (Sep–Oct)
55°–50°W 5°–10°N	NODC	34.6, $n = 76$	27.2, $n = 102$	32.7, $n = 105$	28.4, $n = 193$
	ANACONDA	No data	28.4, $n = 1252$	28.4, $n = 409$	31.2, $n = 1230$
	HYCOM	34.7	32.5	32.0	33.2
	NODC-ANA	No data	−1.2	4.3	−2.8
	NODC-HY	−0.05	−5.32	0.71	−4.8
55°–50°W 10°–15°N	NODC	35.5, $n = 81$	34.9, $n = 99$	34.6, $n = 129$	35.1, $n = 113$
	ANACONDA	No data	31.0, $n = 584$	33.9, $n = 44$	34.3, $n = 298$
	HYCOM	34.9	34.5	34.1	34.6
	NODC-ANA	No data	3.9	0.7	0.8
	NODC-HY	0.5	0.4	0.5	0.5
60°–55°W 10°–15°N	NODC	35.5, $n = 103$	34.7, $n = 49$	33.7, $n = 56$	34.9, $n = 71$
	ANACONDA	No data	31.3, $n = 695$	33.4, $n = 559$	29.1, $n = 815$
	HYCOM	34.9	34.8	34	34.2
	NODC-ANA	No data	3.4	0.3	5.8
	NODC-HY	0.6	−0.1	−0.3	0.7
50°–45°W 5°–10°N	NODC	35.5, $n = 88$	35.8, $n = 30$	33.0, $n = 43$	34.2, $n = 94$
	ANACONDA	No data	35.1, $n = 419$	34.5, $n = 28$	33.6, $n = 1110$
	HYCOM	35.4	33.8	31.4	33.1
	NODC-ANA	No data	0.7	−1.5	0.6
	NODC-HY	0.1	2	1.6	1.1

[a]NODC, ANACONDAS, and model (1979–1998) average salinity within boxes. The differences between the NODC and ANACONDAS cruise data are shown, as are differences between NODC and HYCOM simulations.

[14] Additionally, physical, biogeochemical, and biological measurements were collected in the Amazon Plume region as part of the ANACONDAS field campaigns in May–June 2010, September–October 2011, and July 2012. Underway salinity, vertical profiles of temperature and salinity, and hull mounted RDI WorkHorse Mariner 300 kHz acoustic Doppler current profiler derived vertical profiles of velocity are used here for comparison with the model.

3. Model Validation

3.1. Model-Data Salinity Comparisons

[15] The model simulates the observed seasonal pattern of surface salinity associated with plume discharge, ITCZ meridional migration, and western boundary current transports (Figure 2). Generally, the cruise data (Figures 2e–2h) have a fresh bias relative to the historical archive, which may reflect the goals of the ANACONDAS cruises which were biased toward plume studies. For consistency with prior studies, we define the plume by the 35 isohaline [*Hu et al*., 2004].

[16] Winter (January–February; Figures 2a and 2e) salinity is generally above 34 throughout the plume region except adjacent to the river mouth. The late spring model plume (Figures 2b and 2f) is directed primarily northwestward, separating from the coastline near 6°N, 53°W in the region of a topographic feature, the Demerara Rise, that extends northward from the continental shelf at a depth of about 1000 m. It is not known whether the Rise contributes to the location of the plume departure from the coast, as it is colocated with the northernmost position of the ITCZ. The spring ANACONDAS observations show a significantly fresher plume extending northward than in the model, the historical database or the historical analysis of *Lentz* [1995] (Figure 2f). This may have been a consequence of extreme flooding in the Amazon River through 2009 [*Chen et al*., 2010; *Marengo et al*., 2011], leading to residually fresh western tropical North Atlantic conditions in 2010. The PIRATA moorings at 8°N, 38°W show the lowest surface salinities (reaching 31.5) of the entire record in 2009 and 2010 suggesting far field impact of the Amazon flood (not shown; but see http://www.pmel.noaa.gov/pirata/gif/sal_8n38w_ng.gif). These interannual variations in freshwater discharge are not represented in the model. In summer (Figures 2c and 2g), the NBC retroflection is strong, leading to low salinity water north of 10°N, and extending east along 7°N. The retroflection is fully developed in fall (Figures 2d and 2h), though the Amazon discharge is weakening.

[17] Quantitative comparisons of the mean salinity from the World Ocean Database, the ANACONDAS cruises, and the model averaged over boxes (Figure 2e and Table 1) demonstrates the fresh bias in the cruise data from 2010, 2011, 2012 relative to the historical database. We use the mismatch between cruise and historical salinity estimates as a proxy for in situ variability. Generally, the mismatch between model and historical data is less than or similar in magnitude to the in situ variability, suggesting that the model error cannot be further constrained by the data.

[18] To evaluate the model representation of the plume's vertical and horizontal structure and seasonal variability, we compare vertical profiles of salinity colored by month from the model to observed vertical profiles in four regions (Figure 3). Figure 1 illustrates the location of the regions within which the comparisons are conducted with the historical ship tracks overlain. The regions are chosen to maximize data density, and also to capture the seasonal structure of the waters entering the plume region (region 1), the near field plume (region 2), the retroflection of the NBC (region 3), and the NECC at the PIRATA mooring (region 4).

[19] The inflow of equatorial water into the plume region 1 shows little seasonal and interannual variability in

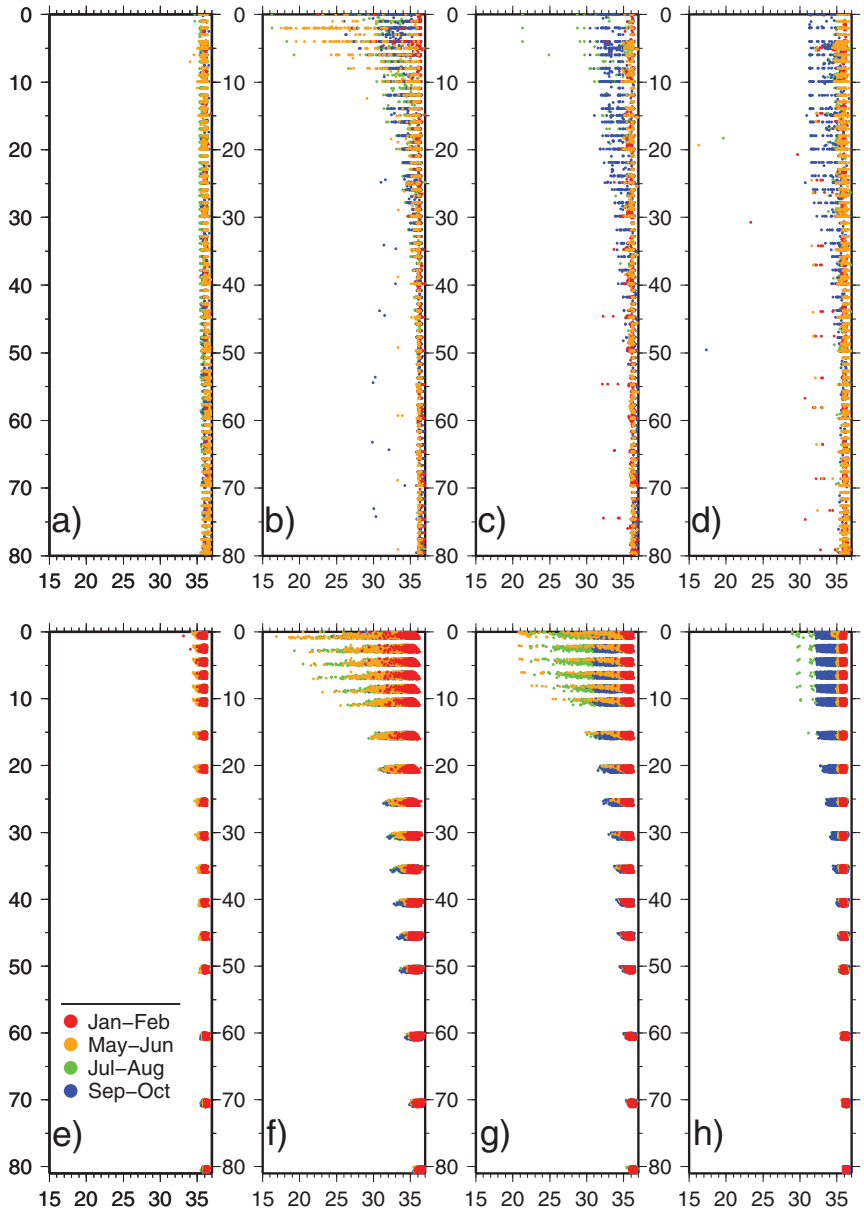

Figure 3. Comparison of vertical salinity profile data for (a–d) the upper 80 m from historical ship observations and (e–h) 1 year of model output (a and e) randomly subsampled for the inflow region 1, (b and f) coastal plume region 2, (c and g) near field retroflection region 3, (d and h) central basin NECC region 4.

salinity in the upper 80 m in either the model or observations (Figures 3a and 3e). The model has a small (∼1) spring fresh bias at the surface.

[20] Greater seasonal variability is observed in region 2 where the plume leaves the coast to flow either northward in winter, or eastward in summer-fall. Observed profiles show seasonal variability extending to 30–35 m depth, whereas the model seasonal variability reaches 50 m (Figures 3b and 3f). The model may be vertically mixing the plume too rapidly. This is also evident in the thickness of the fresh layer ($S > 35.0$) which has a very sharp vertical gradient in salinity in observations, and a weaker vertical gradient in the model. However, the model does display spring and summer surface plume salinities consistent with observations.

[21] In region 3, where the plume migrates eastward offshore seasonally as the NBC retroflection intensifies, vertical mixing deepens the fresh lens in both model and observations (Figures 3c and 3g). The vertical scale of the observed fresh anomaly ($S < 35$) is better matched by the model in region 3 than region 2. Fresh surface salinity is not observed in spring, though the model shows a few fresh profiles, however the observations are biased in this period toward the southern part of the box, and are very limited in this season in any case (Figures 2f and 2g).

[22] As the plume moves well offshore in the NECC (region 4), its thickness increases and the magnitude of the salinity anomaly decreases. Winter profiles (January–February) (Figures 3d and 3h), show oceanic salinity over the entire upper 80 m of the watercolumn, suggesting no plume

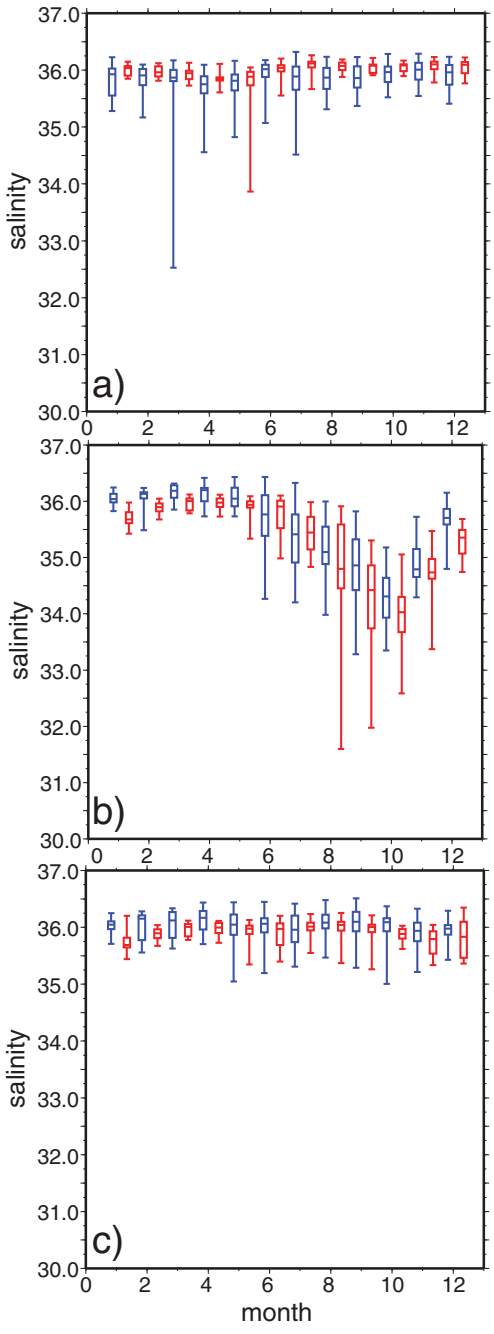

Figure 4. Model (red) and data (blue) salinity box and whisker plots displaying the monthly range, mean, and quartiles of salinity at three PIRATA moorings and the commensurate model locations. The 6 years of data with fewest gaps (1999–2004) are used to avoid systematic biasses associated with the timing of gaps, and so six years of model (1982–1987) are also shown. (a) 0°N, 35°W surface salinity, (b)8°N, 38°W surface salinity, (c) 8°N, 38°W 40 m salinity.

influence during those months. These observations are consistent with the PIRATA mooring data (Figure 4), which shows oceanic surface salinity conditions and little variability in December–May. Fresh surface influence is felt in summer and fall, with the freshest fall surface salinities reaching 31 in the observations, and 32 in the model and these influences extend to 40–50 m in data and model profiles.

[23] Given the limited spatial and temporal coverage from historical data, we compare the model seasonal cycle and variability in salinity with more temporally extensive PIRATA mooring data. The equatorial mooring (35°W, 0°) is chosen to represent the inflow waters into the region prior to plume influence and the 38°W, 8°N mooring is located in the path of the NECC. When the full PIRATA mooring period is compared with the full model period, the model has much higher salinity variability than is observed (not shown). However, systematic biases in data coverage and different analysis periods generate most of this variance. If we use a 6 year daily record (1999–2004) that minimizes data gaps in the PIRATA record, and compare this time series to a 6 year model record, the mean and variance of the model-data comparison is much improved (Figure 4).

[24] Relatively, little seasonal variability (mean range is 0.29 (0.33) for data (model)) is observed in the equatorial inflow to the Amazon Plume region (Figure 4a; normalized model-data root mean square error (NRMSE) = 0.44, average bias = −0.13) as expected from the historical profiles (Figures 3a and 3e). Generally, the model quartile range is smaller than the observed surface salinity distribution, and both model and data show a slightly fresher surface layer ~36.25 in March to May with higher salinity variance. The variability in the inflow to the western tropical Atlantic is however, insignificant compared with the salinity variability in the plume region.

[25] In the region of the NECC, the seasonal cycle in surface salinity is evident in both model and PIRATA mooring observations (Figure 4b; NRMSE = 0.17, bias = 0.26). From January through June, the region experiences surface salinity values of 35.7 or higher, with relatively low variability. The model exhibits a small fresh bias (0.18) during this period, and a 1 month delay in the return to oceanic salinity conditions. In July–December, mean salinity decreases, and salinity variability increases.

[26] Salinity at 40 m depth at the PIRATA 8°N, 38°W mooring are used to illustrate vertical mixing of the fresh anomaly (Figure 4c; NRMSE = 0.62, bias = 0.12). The observations indicate little mean seasonal variability at this location. However, the range of salinity variability increases in the period when the fresh anomaly is present at the surface in both the model and the data, suggesting that mixing to 40 m is rare, but does occur.

3.2. Model-Data Transport and Ring Comparisons

[27] As an indication that the model captures the seasonal cycle in the major currents of the western Atlantic, model upper layer transports are calculated across 44°W from the equator to 10°N and for isopycnals shallower than $24.5\sigma_\theta$ and compared with direct observations [*Bourlès et al.*, 1999a, 1999b] (Table 2). Eastward transport is integrated to estimate the NECC transport, and westward transport is integrated as the NBC transport. Seasonal variations in NBC transport in both model and observations are small relative to the mean transport. In contrast, the NECC model transport has a stronger seasonal cycle consistent with Sverdrup dynamics and observations of *Lumpkin and Garzoli* [2005]. The observations of NECC transport generally

Table 2. Observed and Modeled NBC and NECC Transports[a]

Date	NBC Observed	NBC Model	NECC Observed	NECC Model
Jan 1990, 1991	11.0, 10.2	12.8, range = 6.1–19.7	3.5[b], 10.2[b]	10.4, range = 3.5–17.0
Apr 1996	19.2	11.1, range = 5.7–18.2	23.3	7.7, range = 2.2–15.1
Jun 1991	12.5	10.7, range = 4.9–18.5	17.0	11.7, range = 7.0–21.9
Aug 1989	13.8	11.3, range = 5.3–18.6	17.6	15.6, range = 8.0–23.4
Sep 1990, 1991, 1995[c]	11.5, 14.3, 8.1	11.1, range = 5.6–22.4	18.9, 20.6, 9.8	15.6, range = 7.8–22.1
Average	12.2	11.3, range = 3.9–23.8	18.5 (14.6[d])	11.9, range = 1.0–26.5

[a]Volume transports from *Bourlès et al.* [1999a, 1999b] and the model mean and range over 19 years in Sverdrups (1×10^6 m^3 s^{-1}) across 44°W above 24.5 σ_θ.
[b]The current was not fully crossed.
[c]Section was at 45°W.
[d]Including the January estimates.

cover the latter half of the year when model and wind fields would indicate greater seasonal transport. The January sections unfortunately did not completely cross the current, so the degree to which they underestimate the flow is unknown. The model transports are generally consistent with the observational estimates.

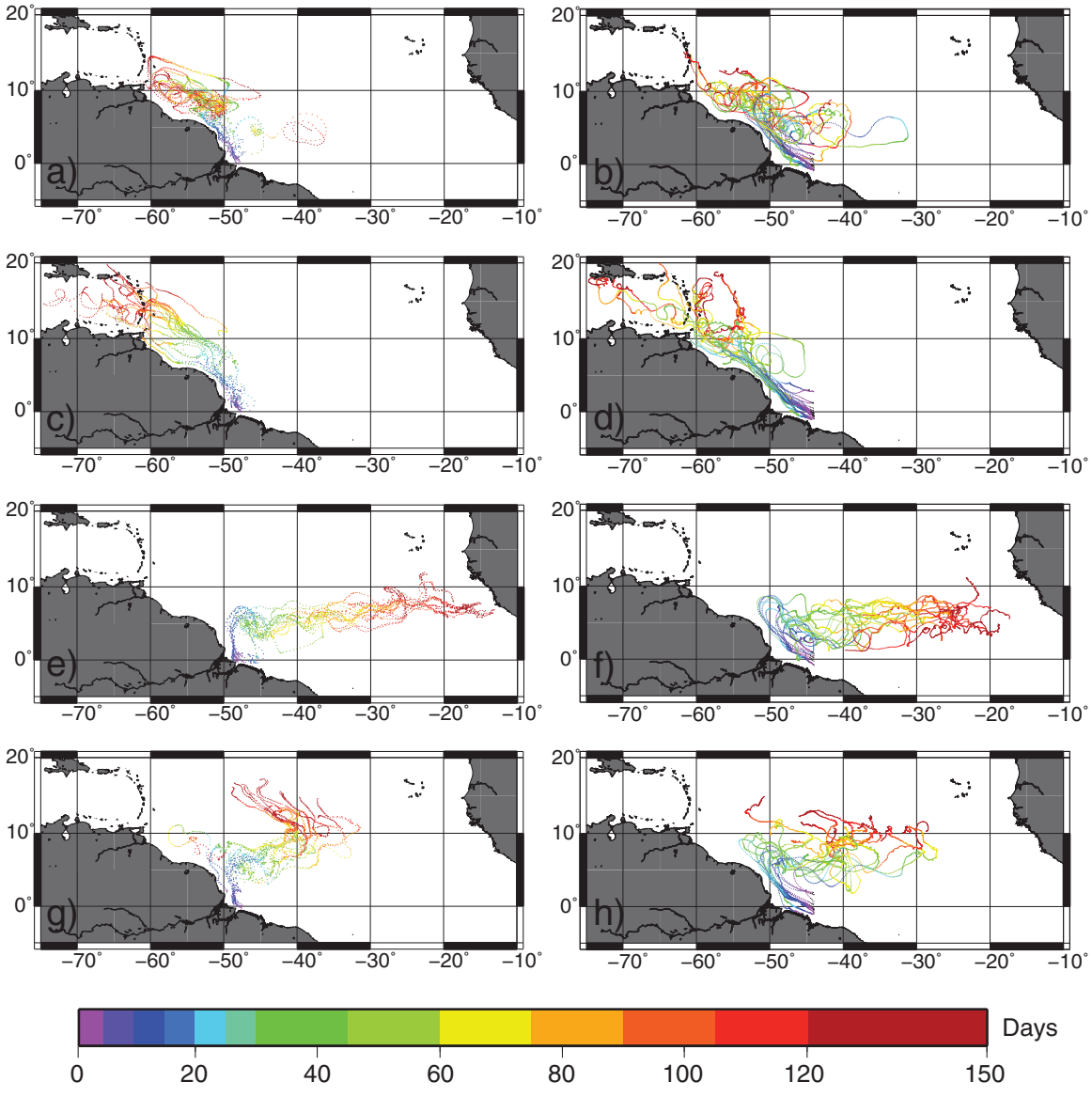

Figure 5. (a, c, e, and g) Selected surface drifter trajectories illustrating the four model pathways. (b, d, f, and h) Selected observed surface drifters which enter the region of the river mouth between 1997 and 2011. Colors indicate the time in days since the drifter was at the mouth of the Amazon.

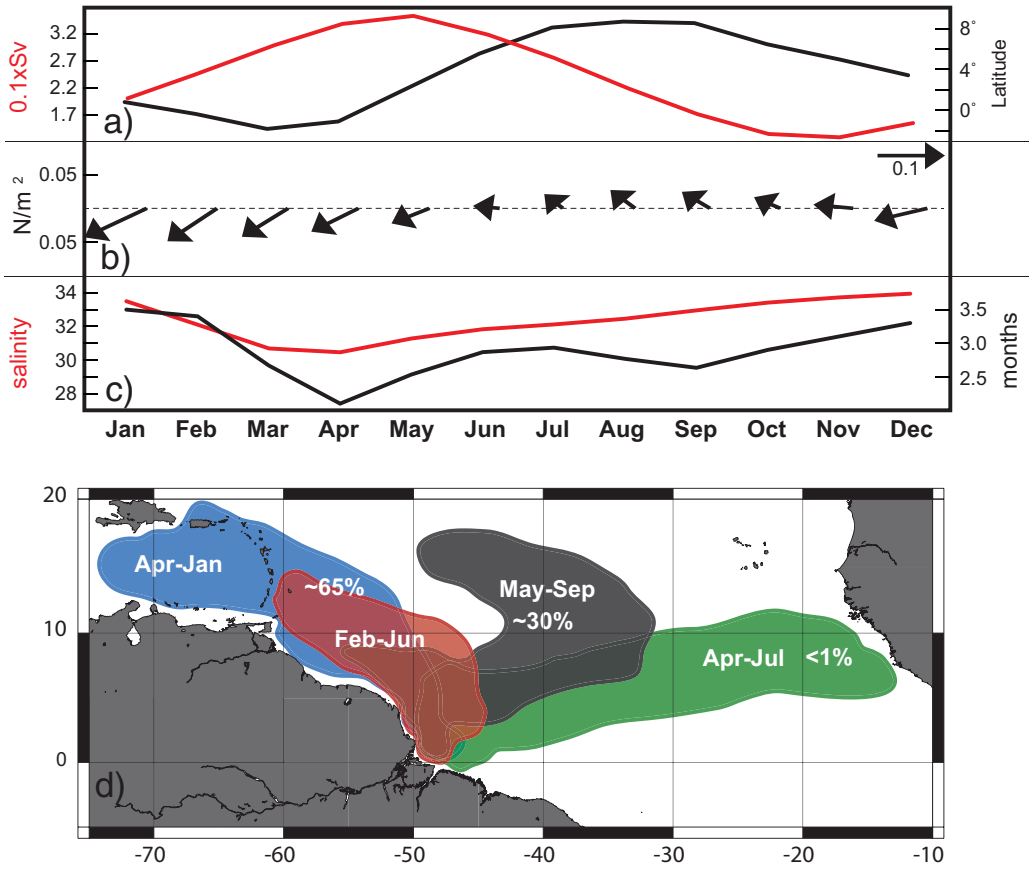

Figure 6. (a) ITCZ position (black line) based on precipitation estimates of *Xie and Arkin* [1997], adapted from *Chiang et al*. [2002] and Amazon climatological discharge from the Brazilian hydroelectric power measurements (red line). (b) Climatological wind stress (5°N, 50°W) from the Southampton Oceanographic Center database. (c) Plume age based on mean age of model drifters within the plume (black line). Average plume salinity within the 35 model isohaline (red line). (d) Schematic of float transport pathways with primary month range for initialization, and the percentage of drifters that follow each pathway. Four percent of drifters remain within the tropical Atlantic for >150 days.

[28] As a final indication of model variability, we calculate the model North Brazil Current Ring formation rate [*Johns et al*., 1990; *Fratantoni and Richardson*, 2006]. Following *Garraffo et al*. [2003], surface expressed rings are detected through analysis of the model meridional mixed layer velocity variations over time. *Garraffo et al*. [2003] find 6 surface rings per year in their 1/12° model study, as compared with the altimetric analysis of *Goni and Johns* [2001] who find 5.7 rings per year. This study with coarser model resolution finds 4.65 surface rings per year, with a range of 3.4–5.8 rings per year in different 5 year periods. Thus, the model has 25% lower ring formation than observed, however there is a lot of variance in the model, with the periods from 1984 to 1987 and 1989 to 1994 having low ring formation rates.

4. Plume Pathways and Influence on the Tropical Gyre

4.1. Plume Pathways

[29] Previous efforts to identify the pathways through which Amazon Plume water reaches the Caribbean used historical hydrographic data to show seasonality in the path of the plume [*Lentz*, 1995], with northward flow in winter and spring, and eastward flow in the NECC during summer and fall. *Hellweger and Gordon* [2002], investigating the time scale for this flow, found a 2 month lag between Amazon discharge and surface salinity at Barbados (59.5°W, 13°N). *Hu et al*. [2004] found a 1 month lag between river discharge and mean plume CDOM concentration based on remote sensing estimates, and determined an average plume translation speed of 0.35 m s^{-1}.

[30] Four pathways are identified with selected model and observed trajectories illustrating these pathways (Figure 5). The indirect northwest pathway (Figures 5a and 5b) exports floats from the tropical Atlantic throughout the year in both observed and modeled trajectories. However, this pathway is most common for floats initialized in February–June. A number of these model and observed drifters become trapped within what was formerly known as the Demerara eddy region (55°W, 8°N) downstream (northwest) of the Demerara Rise. The indirect northwest pathway is distinguished from the more direct northwest pathway (Figures 5c and 5d) by much longer residence time in the NBC region and characteristic looping behavior.

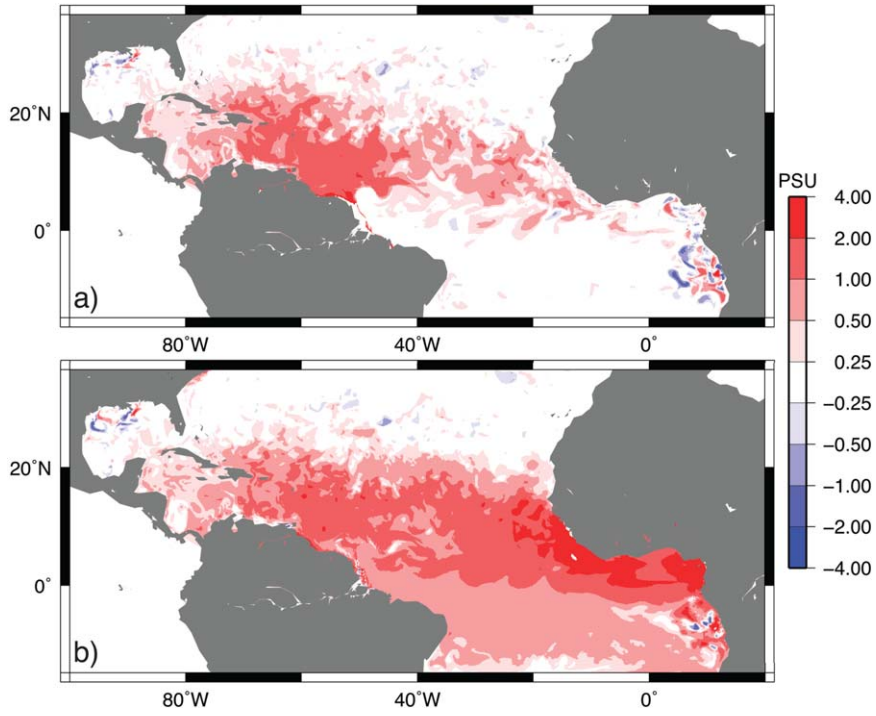

Figure 7. Surface salinity anomaly in January after 4 model years (1983) for (a) noriver-control experiments and (b) noprecip-control experiments.

[31] The direct northwestward trajectories (Figures 5c and 5d) advect rapidly northwestward out of the region with less looping behavior, and many fewer floats becoming stranded at the coast. This pathway is present predominantly for drifters initialized in April through January. A strong coastal current (the Guyana Current) is evident with a roughly 60 day advection timescale between the river mouth and the Caribbean Archipelago, and this coastal trajectory follows the coastline very closely in both model and observations. A second pathway initiates between 50°W and 55°W, where some model and observed floats separate from the coastline to follow the north-south trending edge of the Demerara Rise. These still continue into the Caribbean Archipelago, though some continue northward on the outside of the island chain. This is a relatively short and direct route for plume water into the Caribbean, with time scales of <3 months.

[32] The eastward pathway is most common in April–July initiated trajectories (Figures 5e and 5f). This pathway follows the retroflection of the NBC into the NECC and drifters are carried rapidly toward Africa. Relatively few drifters reach east of 20°W before the NECC weakens in late fall however. A larger fraction of eastward flowing drifters are carried eastward past 38°W, but are ultimately advected northward across 10°N.

[33] May–September initialized trajectories tend to follow the interior subtropical gyre pathways illustrated in Figures 5g and 5h. The Amazon River discharge is weakening at this time (Figure 6), but the NECC remains at its maximum transport. Drifters are rapidly advected eastward away from the river mouth in the NBC and NECC, however as they reach 40°W–35°W after 40–60 days, the NECC begins to weaken, and they are carried northward in the prevailing Trade Wind driven Ekman transport.

[34] These trajectories, which overlap in space and time, suggest that the plume cannot be treated as a coherent structure with uniform age and response to forcing. Rather, the plume is sheared apart by interaction with different current structures and multiple pathways for plume water exist concurrently. Although the direct and indirect northwest pathways, as well as the subtropical gyre pathways may ultimately enter the Caribbean or western subtropical gyre, they have very different time scales. Consequently, although water masses associated with drifters in each pathway still retain lower salinity water than the ambient subtropical gyre, they have rather different physical and, presumably, biogeochemical characteristics as a result of their differing histories.

[35] Plume pathways and properties along with the drivers determining plume distribution are summarized in Figure 6. These elements include the meridional position of the ITCZ, and the climatological local wind stress [*Josey et al.*, 1999]. In December–April, the ITCZ is at its southernmost extreme (Figure 6a), leading to onshore winds that blow the river plume against the continental margin near the river mouth (Figures 6b) inhibiting entrainment into the NBC and limiting plume spread to the slower indirect northwestward pathway (Figure 6d). Up to 80% of the floats initialized at this time run aground. In spring (April–May), Amazon discharge peaks as the ITCZ starts to migrate north, relaxing onshore winds, and the plume begins to spread into the North Brazil and Guyana Currents leading to rapid spreading of freshwater in the direct northwestward, and eastward pathways into the tropical region (Figure 6d). In summer, (June–July), discharge begins to slow as the ITCZ reaches its northernmost point, intensifying the surface expression of the NECC and driving a retroflection of the

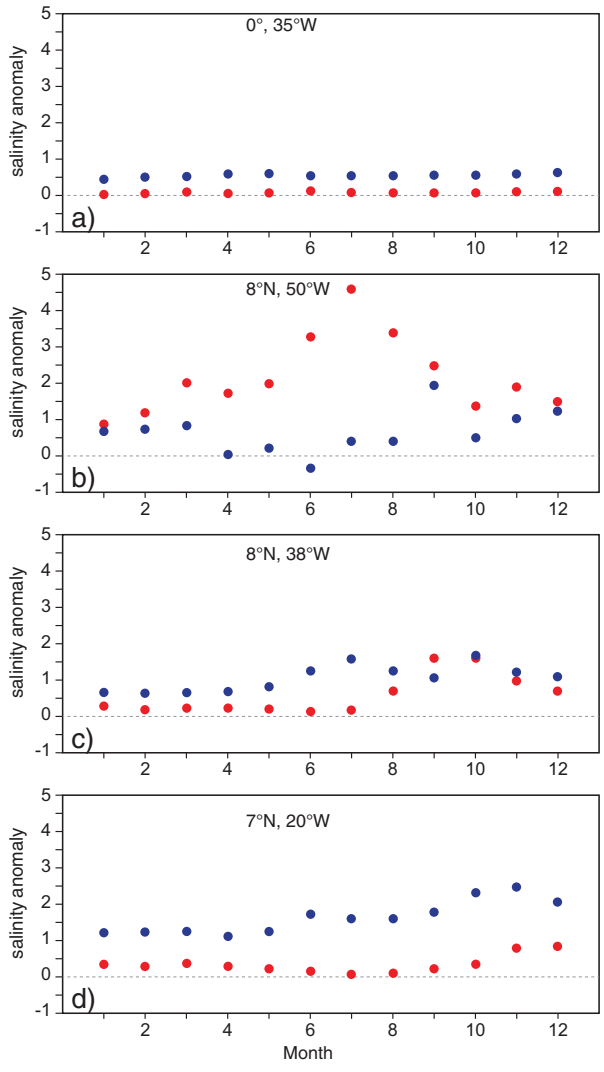

Figure 8. Time series of surface salinity anomaly for noriver-control (red), and noprecip-control (blue) at selected locations: (a) inflow region, 0°N, 35°W, (b) northwestern plume pathway region, 8°N, 50°W, (c) eastward pathway region, 8°N, 38°W, (d) eastern boundary of the eastward pathway region, 7°N, 20°W.

NBC to feed the NECC and increase eastward and interior subtropical freshwater pathways. Less than 15% of the floats initialized at this time run aground. In fall, (August–December), river discharge decreases to its minimum, and the ITCZ moves southward reducing the surface NECC and retroflection. Ekman flow drives plume freshwater north then west in the interior gyre pathway as the North Equatorial Current subtropical return flow moves southward. Mean plume salinity and age, defined as the average time since deployment of drifters within the model plume region, are illustrated in relation to river discharge and winds in Figure 6c and described further below in section 6.1.

4.2. Plume Influence on Salinity in the Tropical Gyre

[36] Both *Ferry and Reverdin* [2004] and *Hu et al.* [2004] made the point that local rainfall was insufficient to create the fresh tropical salinity signature associated with the NECC, however rainfall associated with the ITCZ and evaporation variability have been implicated in the salinity balance and variability of the central tropical North Atlantic in other studies [e.g., *Grodsky et al.*, 2006; *Foltz and McPhaden*, 2008]. To compare the relative roles of ITCZ precipitation and river discharge in setting the tropical Atlantic surface salinity, we conduct three experiments. The control run is similar to the run described previously, however surface and boundary salinity relaxation are eliminated. In the noriver run, the Amazon and Tocantins rivers only are removed from the control run. In the noprecip run, tropical precipitation from the equator to 10°N is eliminated from the control run. All three experiments extend for 5 years, though we highlight only results from the start of the 5th year. Longer simulations are inappropriate for this comparison, because boundary influences and dynamical effects of changing the surface density field become increasingly important.

[37] The difference between the noriver and noprecip runs and the control run illustrates the importance of both precipitation and river discharge to maintaining relatively

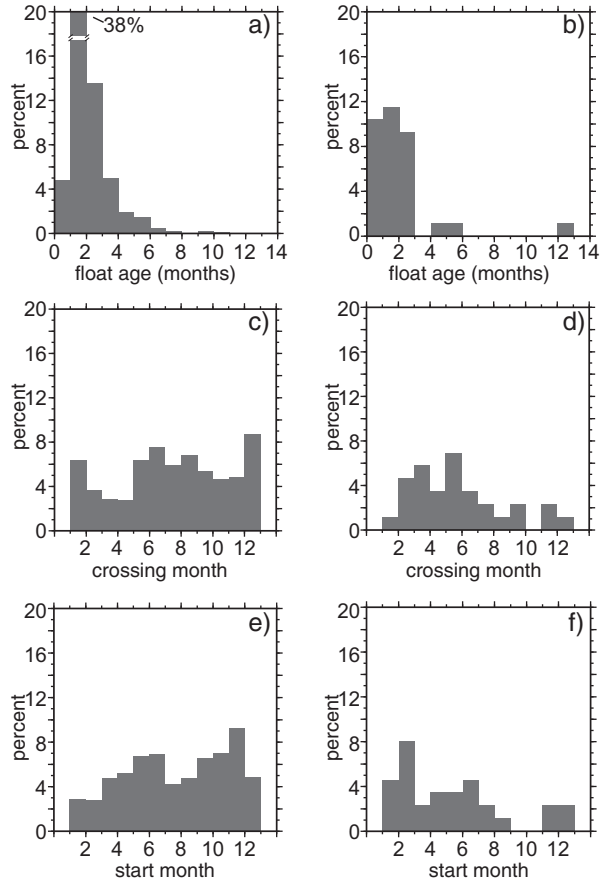

Figure 9. Histograms of float properties in the direct and indirect northwestward pathways (crossing north of 10°N and west of 50°W within 150 days). (a) Model floats in each age bracket. (b) Observed drifters in each age bracket. (c) Model floats crossing in each month. (d) Observed drifters crossing in each month. (e) Starting month for model floats. (f) Starting month for observed drifters.

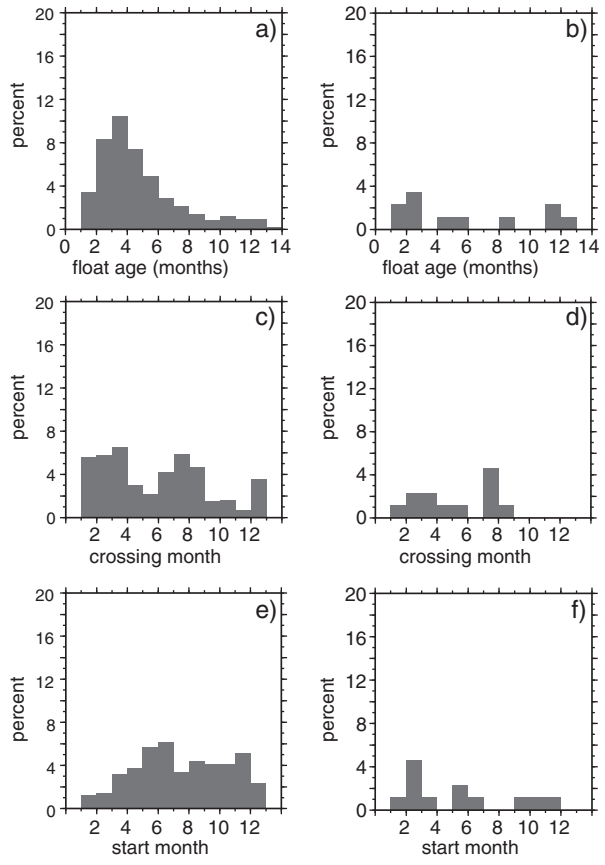

Figure 10. Histograms of float properties in into the Caribbean (west of 61.7°W, between 10°N and 18.5°N) within 150 days. (a) Model floats in each age bracket. (b) Observed drifters in each age bracket. (c) Model floats crossing in each month. (d) Observed drifters crossing in each month. (e) Starting month for model floats. (f) Starting month for observed drifters.

fresh tropical Atlantic surface salinities (Figure 7). The riverine and precipitation influences on surface salinity are profound, with both simulations demonstrating salinity anomalies from 1 to 4 after 4 years over broad reaches of the tropical Atlantic. The riverine influence is strongest in the western tropical North Atlantic, west of 40°W, though eastward propagation of salinity anomalies is evident across the basin as far as the westernmost Gulf of Guinea. Precipitation very strongly influences surface salinity in the Gulf of Guinea, and also contributes across the basin to freshening the upper layer between the equator and 20°N.

[38] The relative contributions of river and precipitation to seasonal surface salinity anomalies are evident by comparing time series of model salinity anomalies at locations across the basin (Figure 8). In the inflow region (Figures 1 and 8a), eliminating riverine inflow has only a very modest ($<$0.25) effect on surface salinity. Equatorial and northern hemisphere rainfall do, however, have an impact on the inflow region surface salinity ($\sim$0.5), though with little seasonality, suggesting that the seasonality of ITCZ rainfall has been damped by advection across the basin in the South Equatorial Current. This is consistent with the very low seasonal salinity variability observed in the model and at the PIRATA mooring at this location (Figure 4a).

[39] Along the northwestern pathway of the Amazon Plume (Figure 8b), the noriver run has greater seasonal and net salinity impact, with the largest anomalies (4.5) expressed in July, 2 months following peak Amazon discharge (Figure 6). The noprecip run influence is largely nonlocal, with anomalies of comparable magnitude to those found in the inflow region, though in September, when the ITCZ reaches its northernmost position, the local precipitation influence increases, with anomalies approaching the noriver run.

[40] Precipitation anomalies along the eastern pathway (Figures 1 and 8c) are similar to the inflow region through winter and spring with precipitation increasingly important as the ITCZ moves northward in June–December. Riverine impacts on the eastern pathways are modest through the winter and spring also until the NBC retroflection initiates in spring. The river influence lags the local precipitation associated with the ITCZ migration and the development of the NBC by 2 months, indicating a roughly 2 month advection timescale. Through late summer and fall, the riverine influence on salinity is of comparable magnitude to the influence of precipitation, with anomalies $>$1.5.

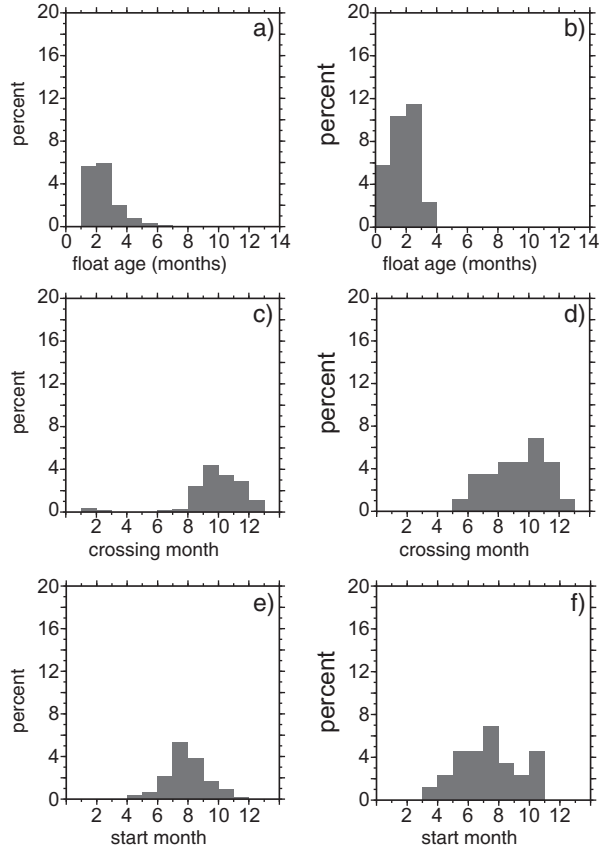

Figure 11. Histograms of float properties in the interior subtropical gyre and eastward pathways (crossing east of 38W within 150 days). (a) Model floats in each age bracket. (b) Observed drifters in each age bracket. (c) Model floats crossing in each month. (d) Observed drifters crossing in each month. (e) Starting month for model floats. (f) Starting month for observed drifters.

Comparison of the magnitude of the noprecip salinity anomaly (1 unit) with the absolute salinity at the PIRATA mooring (Figure 4b), demonstrates that the 1 unit of the total salinity decrease (36–34) beginning in June can be ascribed to precipitation effects. The noriver run salinity anomaly of 1.25 unit begins in August, which then further decreases model salinity at the location of the PIRATA mooring as a result of the Amazon plume (Figure 4b).

[41] Across the basin near Africa (Figure 8d), precipitation dominates the salinity anomaly throughout the year, with a maximum in November. The influence of the Amazon River plume is not insignificant however, particularly in November and December when the riverine salinity anomaly reaches 1.

[42] Thus, both precipitation and the Amazon River plume are important to freshening tropical salinity, with the river dominating in the west, and precipitation more broadly distributed over the basin, leading to greater influence near Africa.

5. Plume Export From the Region

[43] To understand the export of Amazon River water out of the tropical western North Atlantic, we examine the properties of model and observed floats that leave the domain. In particular, we identified two regions of export for plume water northwestward flow out of the tropics in the western boundary region (indirect and direct), and eastward flow across the basin toward Africa (interior gyre and eastward pathways) (Figure 6). We also discriminate between flow to the north into the subtropical gyre, and flow into the Caribbean, as the impact of Amazon Plume water in the enclosed marginal seas on the Caribbean and Gulf of Mexico has important biogeochemical implications. Four years (1979, 1985, 1991, and 1992) are analyzed representing different model NBC transport conditions: low transport/low seasonal amplitude; low transport/normal seasonal amplitude; normal transport/normal seasonal amplitude; high transport/normal seasonal amplitude, respectively. The model drifters are uniformly distributed over time, however the 79 observed drifters are biased by season of initialization with 27% of the drifters initiated in December–February, 20% initialized in March–May, 36% initialized in June–August, and 18% initialized in September–November. We focus therefore, only on the patterns in the observed drifters that are inconsistent with the model, such as observed export during a period when the model has none.

[44] The age distribution for floats crossing 10°N west of 50°W is rather narrow (Figures 9a and 9b), with most floats younger than 3 months when crossing suggesting that the direct path into the northern subtropical gyre has little lag, and is more common than the slower indirect pathway. Sixty-five percent of all drifters leave the tropical Atlantic along this route. The indirect northwestward trajectory is also represented in ages 6 months and more. In the model, this pathway is open throughout the year (Figures 9c and 9d), however there is a general trend to less export in spring, with greater plume export during the rest of the year. The observed floats similarly show some export throughout the year, but in fact show a maximum in spring. However, this export is likely biased because more

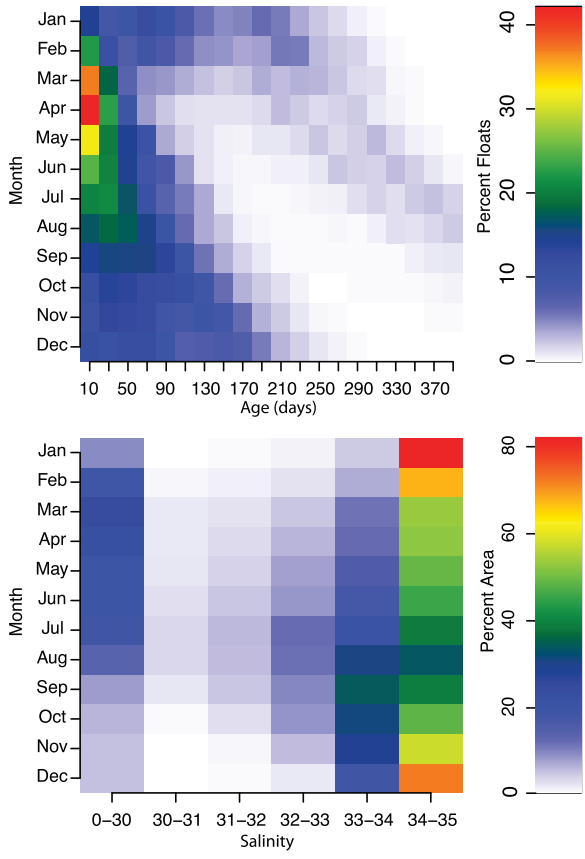

Figure 12. Four years of model trajectories and surface salinity within the plume ($S < 35$) are combined in monthly bins. (a) histograms of the distribution of plume age (percentage of plume drifters in each age bin) in each month. (b) histograms of plume surface salinity (percentage of area in each bin) in each month. Note: the salinity bin width is nonlinear.

observed floats were initialized in winter and thus crossing between February and June. The distribution of floats crossing 10°N as a function of their initialization date is relatively uniform with 4–10% of floats initialized in all months crossing 10°N (Figures 9e and 9f). The exception is for floats initialized in winter and midsummer, which show a drop in crossing rate. This occurs during the periods when floats are either penned up against the river mouth, or cross the Atlantic toward Africa, and thus fewer move northward into the subtropical gyre.

[45] The input of Orinocco and Amazon Plume water into the Caribbean and Gulf of Mexico has been linked to blooms of harmful algae and *Trichodesmium* spp., and reduced water clarity [*Corredor*, 2003; *Coles et al*., 2004]. The timing and magnitude of inputs of Amazon River water into the Caribbean has been studied previously [*Hu et al*., 2004; *Ffield*, 2005; *Chérubin and Richardson*, 2007]. Here we compare the proportion of Amazon River water entering the Caribbean with that advecting northward to the east of the archipelago or turning eastward in the NECC toward Africa. Of the floats that follow the northwest trajectory, 47% entered the Caribbean (defined as floats that crossed west of 61.7°W, south of 18.5°N.

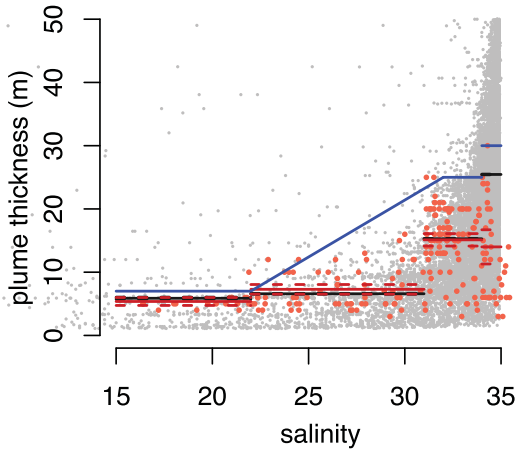

Figure 13. Relationship between plume thickness and surface salinity. Model (gray) based on 4 years of model run (subsampled for plotting only to every 25th value). Uppermost (red) salinity measurements from ANACONDAS (May–June, July–August, September–October) vertical hydrocast profiles with plume thickness determined from the first large vertical salinity gradient. Solid lines (red for observations, black for full model output) are drawn at the mean plume thickness (between salinity ranges 5–22, 22–31, 31–34 and 34–35) and dashed lines at the 95% confidence limits. The relationship described in *Hu et al*. [2004] (blue).

[46] The spread of float ages is greater for floats entering the Caribbean than for the northwest pathway (Figures 10a and 10b versus Figures 9a and 9b). This occurs because the Caribbean inflow includes more floats that became trapped in eddies in the lee of the Demerara Rise (Figures 5a and 5b). Generally, the older floats indicate a saltier plume inflow. The model (Figure 10a) has a peak in the age distribution at 3–5 months, consistent with the analysis of *Chérubin and Richardson* [2007], in which they found remnant plume water to enter the Caribbean several months after its advection north and west of the river mouth. However, the age distribution is broad, ranging from 2 to 6% of floats younger than 2 months, as well as >2% of floats in each age class between 4 and 7 months. Both winter and summer maxima in crossing month are observed in the model floats (Figure 10c) similarly to the 10°N crossing floats. The summer peak is consistent with low salinity observed in the Caribbean during late summer and early fall [*Chérubin and Richardson*, 2007]. These floats are quite young in the model, and thus cross with low salinity. Those that cross in winter are older floats that form the broad tail on the age distribution and they are associated with higher salinity plume water. Figures 10e and 10f show the fraction of plume floats crossing into the Caribbean as a function of start month. While there is a local minimum in December–February, the distribution is quite flat, suggesting that ultimately 4–8% of the river water discharged in each month makes it into the Caribbean.

[47] Floats in the eastward pathway cross 38°W between 1 and 4 months after being initialized at the river mouth, with the majority 1.5–3 months in age (Figures 11a and 11b). Late summer and early fall floats end up crossing 38°W in <50 days on average. As expected, the floats are tightly linked to the seasonal cycle in the surface expression of the NECC. The observed floats show a greater fraction of the total crossing the Atlantic, but again, the bias in initial distribution may influence this result. Most model floats cross 38°W in August–December, with observed floats showing a slightly broader distribution (June–December) (Figures 11c and 11d). This is consistent with the initiation of the retroflection in June, and a 1.5–3 month lag between river mouth and crossing. River discharge between December and April (December–March in the observed floats) is excluded from crossing the basin (Figures 11e and 11f), so river properties associated with the low river discharge period of summer and fall are most likely to influence the eastern Atlantic. The number of floats in the eastward and subtropical gyre interior pathways is low, 30%, with <1% of floats reaching the eastern boundary (20°W). Thus, river export to the eastern Atlantic is smaller than export into the Caribbean and the subtropical gyre.

6. Plume Properties Within the Tropical Atlantic

6.1. Plume Age and Salinity

[48] As a result of the complex seasonality of the tropical currents and Amazon discharge illustrated above, the fresh plume waters in the western tropical North Atlantic are a mixture of Amazon River waters with very different age characteristics. Thus, plume area is only likely to be related to discharge magnitude if salt entrainment is exactly constant along all pathways and over all seasons. In the model, the average age of floats within the plume, defined as salinity <35, varies throughout the year from a maximum of 104 days in January to a minimum of 63 days in April (Figure 6c). Coincident with these changes in plume age are changes in the average salinity of the plume. The minimum in plume salinity (March–April) is roughly coincident with the youngest average plume age, and leads the maximum river discharge by 1–2 months (Figure 6). This minimum cooccurs with the southernmost location of the ITCZ, suggesting that the dynamics of the surface currents and wind are more critical to determining the plume spread and thus regional salinity than the magnitude of the discharge. Plume maximum salinity occurs in fall, September–December, and is broadly distributed. This salinity pattern occurs whether calculated based on drifter salinity, or the areally averaged model salinity, suggesting that the drifters are sufficiently densely distributed to resolve the plume age structure.

[49] In contrast to Figure 6c, *Salisbury et al*. [2011] integrated plume salinity over a box (0°–15°N, 62°–45°W)

Table 3. Plume Thickness as a Function of Surface Salinity for Observations and Model[a]

	$15 \le S < 22$	$22 \le S < 31$	$31 \le S < 34$	$34 \le S < 35$
Model	5.9 m	6.6 m	15.1 m	25.5 m
CTD profiles	5.4 m	7.3 m	15.3 m	14.0 m

[a]Model plume thickness, calculated as vertical salinity gradient >0.2. Observed plume thickness calculated based on the first vertical salinity gradient maximum.

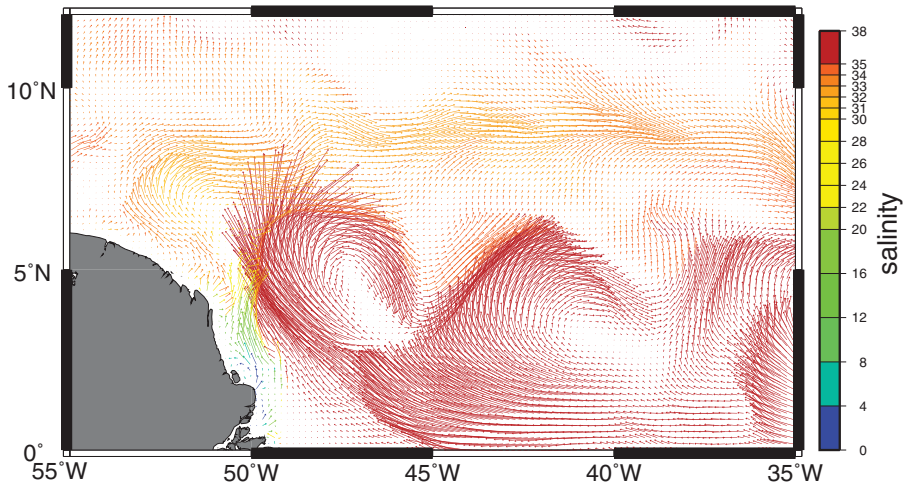

Figure 14. Surface velocity vectors colored by salinity from the model year 1991 in early October.

based on remote sensing salinity estimates and found minimum salinity to occur in June. If we integrate over their domain, we find minimum salinity occurs in July and the model mean salinity is consistently fresher than their satellite based estimates. Because the plume is dynamic with variable boundaries, changes in salinity within their box may reflect changes in circulation, mixing, or discharge.

[50] However, the mean age and salinity of the plume fail to capture the complex pattern of plume evolution. The age distribution of floats within the plume is not uniform (Figure 12a). During January, the distribution is broad and trimodal, with 20% of the floats aged under 20 days, a further 20% aged 60–140 days (initiated in October), and a final 10% aged 200+ days (initiated in July). The oldest January floats that still retain surface salinity <35 were initiated in the previous February. Thus, the winter plume surface is comprised mostly of water from the previous fall and summer. In January, nearly 80% of the plume is in the saltiest category (Figure 12b), reflecting this long period of entrainment and mixing with little new river input.

[51] In March–May, nearly 40% of the plume area is composed of water younger than 20 days. This occurs in part because the Amazon discharge is increasing, but more importantly, southward motion of the ITCZ relaxes the southwesterly trades at the mouth of the river (Figure 6), allowing more river water to become entrained and exported in the NBC. A second maximum at 200–300 days reflects the gradual aging of the previous fall's river water, which still has not been exported out of the western tropical North Atlantic. During this period, the plume salinity (Figure 12b) is bimodal, with 20% of the water fresher than 30.

[52] As the retroflection initiates in June with the northward migration of the ITCZ (Figure 6), the plume begins a gradual aging process. The young mode of the age distribution broadens and expands until October, when the supply of freshwater is reduced, the ITCZ moves southward, and the plume is held up against the coast at the river mouth. During this summer-fall period, the plume salinity distribution broadens in the higher salinity mode. As the plume is stretched and entrained in the NECC, plume age gradually

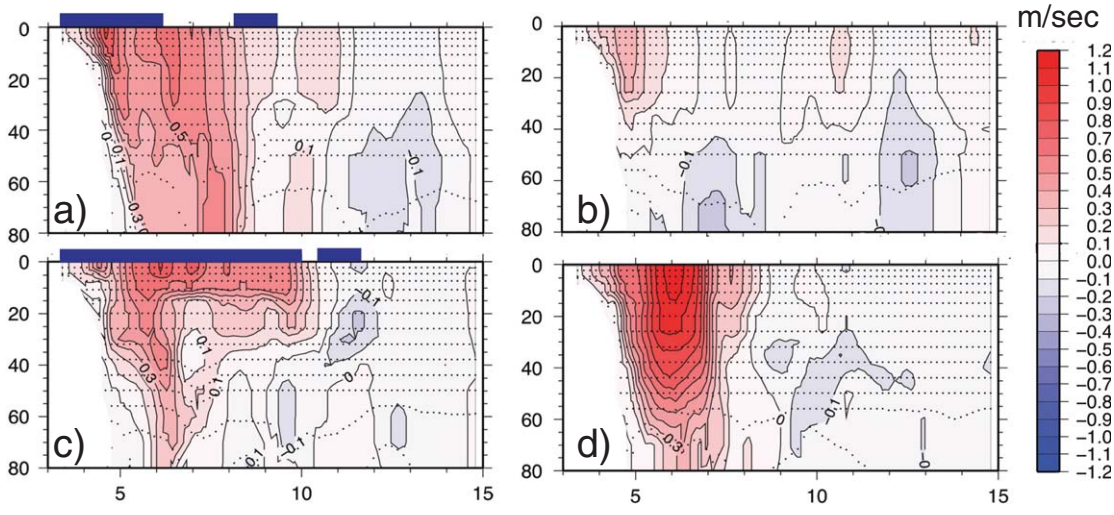

Figure 15. Zonal sections of meridional velocity (m/s) along 52°W. Heavy horizontal blue lines show the regions of plume influence. (a) Control run in June. (b) noriver run in June. (c) Control run in September. (d) noriver run in September.

increases, yet the entrainment and mixing process is reduced, leading to more mesohaline (31–34) salinity water. This may also be due to plume entrainment and mixing with the previous year's plume water.

[53] During the period of low discharge, and unfavorable winds for plume export, the existing plume ages and becomes saltier, until resupply of freshwater is initiated at the coast in January. Thus during most periods of the year, the plume consists of two modes, a young fresh plume, and an older saltier plume from the previous year. However, the broadest range of salinity distributions occur in fall, associated with stretching and rapid advection of the plume, and not with high freshwater input.

6.2. Plume Thickness and Volume

[54] A relationship that relates plume surface salinity and area to volume is of interest given new technology for remote sensing of surface salinity. The model relationship between salinity and plume thickness is very similar to the observed relationship for salinity <34, with the observed values lying over the modeled distributions with similar variance (Figure 13). Although surface salinity was <15 in near shore regions, the river plume extends through the full water column (depths <20 m), thus plume thickness was constrained by water depth rather than plume dynamics, so these values are not included. We do not find statistically significant linear relationships between observed plume thickness and surface salinity and time of year. As a result, we select regions of salinity space with a characteristic salinity mean and variance, and calculate mean plume thickness over each region (Table 3). Model plume thickness is calculated as the distance from the surface to the first vertical salinity gradient >0.2. Observed plume thickness is calculated based on the first local maximum in vertical salinity gradient. At the higher salinity range, 34–35, the model estimate of plume thickness is much greater than is observed. This is likely to be the result of undersampling of the higher salinity plume in the ANACONDA cruises, though it could also be more limited temporal coverage that excludes winter in the observations. Unfortunately, much of the volume of the plume is contained within this salinity range based on the model estimate (Figure 12), and further observations are needed to constrain the thickness variability.

[55] The goodness of fit of the plume salinity to thickness relationship used in [*Hu et al*., 2004] is not shown in their work, so we cannot determine whether this relationship improves on their efforts, however we include their regression in Figure 13. Compared with our late spring, summer and early fall observations, and with the model results, their algorithm would overestimate the freshwater volume in all salinity ranges. They make a correction to surface salinity to estimate average plume salinity which slightly increases the salinity used in their algorithm, however this will tend to further increase the estimate of the plume thickness calculated from a given surface salinity. We note that our measurements were bounded by 15°N and 45°W, whereas many of the float locations used in their calculation were farther from the river mouth, thus its possible that farther from the river mouth, or at higher salinities, their regression may be more consistent with data.

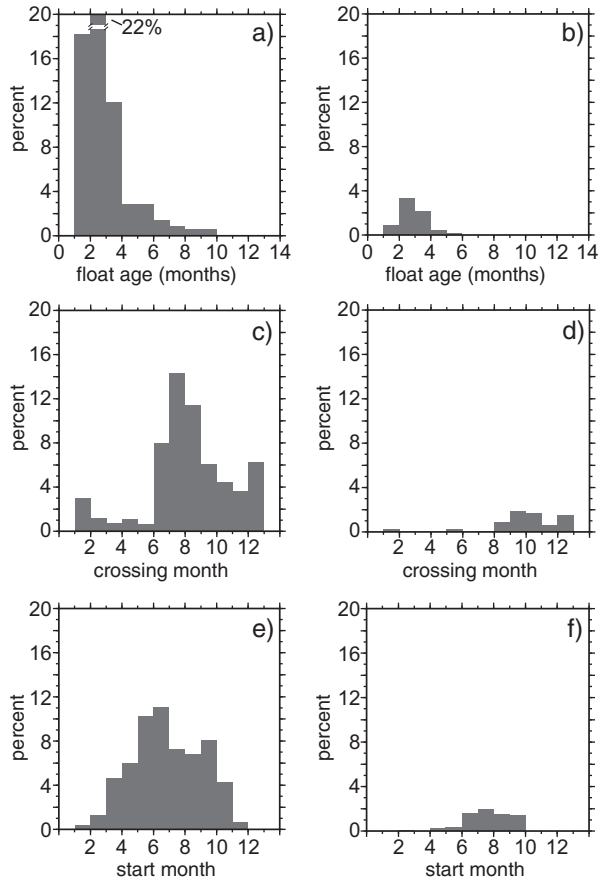

Figure 16. Histograms of the noriver run float properties in the direct and indirect northwestward pathways (crossing north of 10°N and west of 50°W within 150 days). (a) Model floats in each age bracket. (c) Model floats crossing in each month. (e) Starting month for model floats. Histograms of the noriver run float properties in the eastward and interior gyre pathways. (b) Model floats in each age bracket. (d) Model floats crossing in each month. (f) Starting month for model floats.

7. Plume Relationship With Surface Currents

[56] An October 1991 snapshot of the model mixed layer current vectors shown colored by surface salinity (Figure 14) illustrates that while the river plume follows the NBC into the NECC, the plume is not centered in the jet. The NECC jet at 6°N forms a barrier at the surface to the exchange of freshwater across the NECC, and freshwater is seen to exist only on the northern flank of the NECC core except where a meander eddy pinches off. This is why none of the observed or modeled drifter trajectories are found to move into the southern hemisphere, and why the salinity anomaly associated with the noriver-control run is exclusively north of the NECC (Figure 7a). The presence of the NBC and its retroflection effectively prevent Amazon freshwater from crossing south of 6°N in the basin interior. As a result, very sharp salinity gradients are found in the northern NECC.

[57] The existence of multiple NECC cores has been recognized since *Richardson and McKee* [1984]. *Urbano et al*. [2006] explained the multiplicity as a result of the broad,

almost square shape of the westward zonal trade wind stress maximum, which creates two wind-stress curl maxima at each side of the wind stress maximum. The model shows evidence of multiple NECC cores, both in zonal sections, and in the surface current vectors, particularly in fall (e.g., Figure 14). In this case, the southern core acts as a sharp boundary for the freshwater, and the northern core acts as a convergent front intensifying and accelerating the flow of fresh plume water zonally across the basin. The second northern jet tends to be somewhat ephemeral, and not always zonally continuous.

[58] The plume has a dynamical impact on the circulation (Figure 15). Snapshots of the control run show vertical shear particularly associated with the regions of plume influence, suggesting that the Amazon plume influences and intensifies the surface velocity through shoaling the vertical density gradient. In the June snapshot, the elevated freshwater input intensifies the northward flow in the upper 20 m, and broadens the width of the NBC flow. In the September snapshot, the confinement of the NBC to the surface plume region is clear; however, this actually acts to reduce the intensity of the current by broadening it as compared with the noriver simulation. This appears consistent with the previous study of *Masson and Delecluse* [2001], which suggested that the geostrophic component of the NBC retroflection is weakened in the presence of the plume.

[59] We examined the observed current structure along the ANACONDA cruise tracks to see whether plume influenced regions show more vertical velocity shear. At many stations the plume influence is shallow, and if there is velocity shear associated with the plume, it occurs above the shallowest ADCP bin at 11 m (2 m resolution). However, if we select stations at which the plume influence was strong to depths $>$15 m, we can compare the vertical shear in the water column between 15–11 m and 25–20 m depth for stations with and without plume influence. Over the first two cruises, 8 stations have no plume influence, and 10 have plume influence extending to near 20 m. The average magnitude of the velocity shear vector for stations without plume influence (0.11 m/s) is less than half that for stations with plume influence (0.26 m/s). However, the oceanic stations are located farther from the energetic western boundary current regime, so vertical shear in the upper 25 m might be expected to be lower as a result of the mean current structure.

[60] During the fall 2011 ANACONDAS cruise, a strong convergent salinity front was observed in the first NECC meander at 7°N, 49°W with floating debris, and a marked color change in the water (circle in Figure 1). The front was also associated with reduced surface turbulence likely as a result of wave breaking on the density front. Very sharp tracer and particle boundaries at the core of a dynamical jet are observed and have been modeled in other regions, such as particles crossing the Gulf Stream front [e.g., *Bower and Lozier*, 1994]. Across this salinity front, where the plume and the oceanic regions were separated by a few hundred meters, the magnitude of the velocity difference between the two layers changes from 0.26 m/s in plume influenced water to 0.15 m/s in oceanic conditions. Thus, these observations appear to confirm that the plume acts to increase the vertical shear in the upper water column.

[61] This enhancement of vertical shear may be due to trapping of the wind driven momentum flux in the upper plume layers decoupling them partially from the underlying flow. Additionally or alternatively, the salinity gradient may influence the geostrophic balance. *Cronin and McPhaden* [2002], following [*Roemmich and Morris*, 1994], calculated the potential vertical shear enhancement due to a horizontal salinity gradient observed in an analogous region, the western Pacific warm pool. They found that surface currents might be enhanced by 20 cm s^{-1} relative to currents at 50 m depth by a salinity gradient of 0.2 over 100 km. In this region, we routinely observe horizontal salinity gradients in excess of 10 over distances of 100 km. If we make a calculation following their Appendix A, the depth-dependent acceleration would reach 7.4×10^{-7} s^{-2}, and integrated over a 50 m mixed layer depth for 3 days, the enhancement to surface velocity would reach 9.5 m s^{-1}. While increases of this magnitude are clearly implausible, and likely point to the role of ageostrophic dynamics, vertical shear associated with horizontal salinity gradients could reach significant levels such as we observe in the model and observations.

[62] The integrated effect of this dynamical change is clear when comparing the trajectories of floats released into the noriver and control runs. The age of the drifters is increased in the noriver run (Figure 16a versus Figure 9a), with a peak of drifters in the 2–3 month bin rather than the 1–2 month bin, as though the distribution has widened and been shifted by a month. Very few floats cross north of 10°N in the first half of the year in the noriver run (Figure 16c), with the bulk crossing in June–December. The control run had a very modest decrease in 10°N crossings in spring (Figure 9c). The primary reason for the increase in age and change in crossing month is because floats initialized in November–March rarely cross north of 10°N. The river outflow during this period of the year when the river plume is penned up against the coastline is critical to moving floats into the larger scale flow. Examination of the float trajectories (not shown) demonstrates that the coastal current pathway is similar in both experiments. In both simulations, floats become entrained into flows that are offshore, however these flows are much more linear and less dispersive in the noriver run. This continues throughout the year, with the control run distributing floats much more broadly and in less well-defined pathways.

[63] Many fewer floats cross 38°W in the noriver run (Figure 16b) compared with the control run (Figure 11), thus this pathway becomes much less important. Similarly to the northwest pathway, there is a general 1 month increase in the noriver age distribution at the crossing point (Figure 16b) compared with the control run (Figure 11a). There is little change in the seasonality of this pathway in the noriver run compared with the control run.

[64] Thus, the primary integrated impact of the Amazon River on the simulated floats is to increase the time required to exit the tropical gyre by roughly 1 month. Somewhat surprisingly, the noriver simulation is much less dispersive, with particles remaining clumped together over broad regions. As a result of the slower surface flows, fewer floats actually leave the gyre in the year long timespan. The Amazon River is also critical to opening up the north-west pathway in the first half of the year, compared to simulations without the river. Without the Amazon, fewer floats are exported east in the eastern and interior subtropical gyre pathways.

8. Summary and Discussion

[65] We integrate field observations with model simulations to explore the pathways followed by Amazon River water throughout the tropical Atlantic Ocean. Four pathways are identified using observed and modeled surface drifters. The direct and indirect northwest pathways follow the coastline of South America and have rapid 2–3 month and much slower 5–6 month time scales, respectively. The eastward pathway across the basin in the NECC reaches Africa with a time scale of <5 months. The interior pathway into the tropical Atlantic interior advects water into the subtropical North Atlantic after about 4 months, flowing north and westward in the Ekman and NEC flows following the decay of the surface expression of the NECC.

[66] These pathways have seasonal variability, with the northwest pathways open year round, while the eastward and interior pathways are more seasonal because of the influence of the ITCZ migration and its effect on the surface NECC. The seasonal cycle in the magnitude of Amazon discharge is not a primary influence on the plume area or pathways. The youngest and freshest plume occurs in early spring prior to maximum Amazon discharge, and occurs during the southernmost ITCZ position while the plume is pinned against the coastline by the prevailing trade winds.

[67] In the model, river water enters the Caribbean throughout the year, however a summer maximum in inflow contains younger fresher plume water, whereas the lower winter inflow is saltier and older. The river water crossing the basin contributes to low salinity anomalies in November and December at 20°W in the model. This corresponds to Amazon plume water primarily discharged in the high flow April–July flood period and the geochemical properties of that flow may differ from those associated with low flow periods.

[68] River water and precipitation are equally responsible for the seasonal cycle in salinity observed in the central tropical Atlantic Ocean. Thus on decadal and shorter time scales, it is likely that central tropical Atlantic surface salinity responds to changes in the magnitude of river flow, or in the partitioning between pathways taken by the river plume. Indeed, the freshest surface water observed in the 8°N, 38°W PIRATA mooring occurred in 2009 and 2010, following the great Amazon floods that ended in 2009 [*Chen et al*., 2010; *Marengo et al*., 2011]. If Amazon discharge remained constant, but there were changes in the partitioning of freshwater between pathways, then freshening of the central tropical North Atlantic should be accompanied by increasing salinity in the Caribbean and/or western North Atlantic subtropical gyre. This is the pattern described in the 50 year salinity trend analysis of *Durack and Wijffels* [2010], but the coherence of the global trends in western basin tropical salinity in their analysis suggest that at these time scales precipitation associated with the ITCZ may drive trends.

[69] The plume itself, as bounded by the 35 isohaline, is a complex mixture of waters and is not homogeneous in age or salinity. Nor does the entire plume respond similarly to seasonal forcing as a result of the enormous area it covers. Throughout much of the year, the plume is a mixture of recently discharged Amazon River water and waters discharged in the previous year. While the mean plume salinity is lowest in spring, the area of the plume with the greatest span of salinity between 30 and 34 occurs in fall.

[70] We illustrate a relationship between surface salinity and plume thickness based on observations but consistent with model results that could be applied to remote sensing estimates of surface salinity to estimate the seasonal and interannual variability in plume freshwater and nutrient inputs. This relationship, based on three cruises in the western tropical North Atlantic, results in systematically thinner plume estimates than the analysis of *Hu et al*. [2004]. However their estimate may have contained more far-field measurements. Their estimate at higher salinities is closer to the model estimate than the observed relationship. Given the new remote sensing technology for detecting surface salinity, this relationship could provide a means for examining the interannual and seasonal variations in freshwater flux into the tropical Atlantic.

[71] The export of Amazon River water is almost exclusively to the north as a result of the NBC, and NECC jet structures which together act as a barrier to southward flow of river water. The only pathway for plume water to the south requires crossing the Atlantic basin, and southward flow along the African coastline. This however potentially provides a pathway for Amazon River plume water with associated communities and biogeochemical properties to influence the coast of Africa and, ultimately, the southern hemisphere.

[72] *Foster et al*. [2009] showed that the same nitrogen fixing communities associated with the Amazon River Plume are also associated with freshwater in the Gulf of Guinea, which could also suggest connectivity between the regions. Enhancement to surface stratification associated with advection of river water could influence mixed layer depth, and thus SST. The meridional temperature gradient across the zone of upwelling and into the warmer Gulf of Guinea has been shown to influence air-sea interactions in this area of importance to the West African Monsoon and regional climate [*Caniaux et al*., 2011].

[73] Model simulations and in situ ADCP profiles demonstrate that the presence of the plume contributes to increased velocity shear in the upper 20 m in the plume region. This is consistent with both momentum trapping in the shallow plume layer, and with intensification of vertical velocity shear associated with horizontal salinity gradients. This suggests that extrapolation of typical 75 kHz RDI ship hull mounted ADCP derived currents from a first bin at 28 m to the surface to estimate current transport may be missing significant surface trapped flow in this region. Indeed, the 300 kHz instrument used here is likely missing vertical shear where the plume layer is shallower than 5–10 m. Furthermore, simulations without inclusion of the river plume have significantly less eddy stirring and particle dispersal in the surface waters. Thus, the plume itself may contribute dynamically to the eddy variability in the western tropical North Atlantic region.

[74] **Acknowledgments.** We appreciate the thoughtful and significant suggestions of three anonymous reviewers that improved this paper. We thank the captains, crew, and science support staff of the R/V Knorr, R/V Melville, and R/V Atlantis for their support of the scientific goals of the ANACONDAS project. We also thank the TAO Project Office of NOAA/

PMEL, the Global Drifter Program of NOAA/AOML, and the NOAA NODC for providing outstanding data archive and retrieval facilities that facilitate comparisons between models and data. A. Wallcraft of the Naval Research Laboratory generously assisted with model code and fields. This research was supported by grants from the National Science Foundation (OCE-0933975) and The Gordon and Betty Moore Foundation. This is UMCES contribution 4747.

References

Antonov, J. I., D. Seidov, T. P. Boyer, R. A. Locarnini, A. V. Mishonov, H. E. Garcia, O. K. Baranova, M. M. Zweng, and D. R. Johnson (2010), *World Ocean Atlas 2009, Volume 2: Salinity*, edited by S. Levitus, 184 pp., U.S. Gov. Print. Off., Washington, D. C.

Balaguru, K., P. Chang, R. Saravanan, and C. J. Jang (2012), The Barrier Layer of the Atlantic warm pool: Formation mechanism and influence on the mean climate, *Tellus, Ser. A*, *64*, 1–17, doi:10.3402/tellusa.v64i0.18162.

Beardsley, R. C., J. Candela, R. Limeburner, W. R. Geyer, S. J. Lentz, B. M. Castro, D. Cacchione, and N. Carneiro (1995), The M2 tide on the Amazon shelf, *J. Geophys. Res.*, *100*(C2), 2283–2319.

Bleck, R. (2002), An oceanic general circulation model framed in hybrid isopycnic-Cartesian coordinates, *Ocean Modell.*, *37*, 55–88.

Bourlès, B., Y. Gouriou, and R. Chuchla (1999a), On the circulation in the upper layer of the western equatorial Atlantic, *J. Geophys. Res.*, *104*(C9), 21,151–21,170.

Bourlès, B., R. L. Molinari, E. Johns, and W. D. Wilson (1999b), Upper layer currents in the western tropical North Atlantic (1989–1991), *J. Geophys. Res.*, *104*(C1), 1361–1375.

Bourlès, B., et al. (2008), The PIRATA program: History and accomplishments of the 10 first years tropical Atlantic observing system's backbone, *Bull. Am. Meteorol. Soc.*, *89*(8), 1111–1125.

Bower, A. S., and M. S. Lozier (1994), A closer look at particle exchange in the Gulf Stream, *J. Phys. Oceanogr.*, *24*, 1399–1418.

Boyer, T. P., J. I. Antonov, O. K. Baranova, D. R. Johnson, R. A. Locarnini, I. V. Smolyar, and M. M. Zweng (2009), World Ocean Database 2009, in *NOAA Atlas NESDIS 66*, edited by S. Levitus, 216 pp., U.S. Gov. Print. Off., Washington, D. C.

Caniaux, G., H. Giordani, J.-L. Redelsperger, F. Guichard, E. Key, and M. Wade (2011), Coupling between the Atlantic cold tongue and the West African monsoon in boreal spring and summer, *J. Geophys. Res.*, *116*(C4), C04003, doi:10.1029/2010JC006570.

Chassignet, E. P., L. T. Smith, and G. R. Halliwell (2003), North Atlantic Simulations with the hybrid coordinate ocean model (HYCOM): Impact of the vertical coordinate choice, reference pressure, and thermobaricity, *J. Phys. Oceanogr.*, *33*, 2504–2526.

Chelton, D. B., R. A. DeSzoeke, M. G. Schlax, K. El Naggar, and N. Siwertz (1998), Geographical variability of the first baroclinic Rossby radius of deformation, *J. Phys. Oceanogr.*, *28*(28), 433–460.

Chen, J. L., C. R. Wilson, and B. D. Tapley (2010), The 2009 exceptional Amazon flood and interannual terrestrial water storage change observed by GRACE, *Water Resour. Res.*, *46*(12), W12526, doi:10.1029/2010WR009383.

Chiang, J.C.H., Y. Kushnir , A. Giannini (2002), Deconstructing Atlantic Intertropical Convergence Zone variability: Influence of the local cross-equatorial sea surface temperature gradient and remote forcing from the eastern equatorial Pacific, *J. Geophys. Res*., *107*(D1), doi:10.1029/2000JD000307.

Chérubin, L. M., and P. L. Richardson (2007), Caribbean current variability and the influence of the Amazon and Orinoco freshwater plumes, *Deep Sea Res., Part I*, *54*(9), 1451–1473, doi:10.1016/j.dsr.2007.04.021.

Coles, V. J., C. Wilson, and R. R. Hood (2004), Remote sensing of new production fuelled by nitrogen fixation, *Geophys. Res. Lett.*, *31*, L06301, doi:10.1029/2003GL019018.

Cooley, S. R., V. J. Coles, A. Subramaniam, and P. L. Yager (2007), Seasonal variations in the Amazon plume-related atmospheric carbon sink, *Global Biogeochem. Cycles*, *21*, GB3014, doi:10.1029/2006GB002831.

Corredor, J. (2003), Remote continental forcing of phytoplankton biogeochemistry: Observations across the ''Caribbean-Atlantic front,'', *Geophys. Res. Lett.*, *30*(20), 2057, doi:10.1029/2003GL018193.

Cotrim da Cunha, L., E. T. Buitenhuis, C. Le Quéré, X. Giraud, and W. Ludwig (2007), Potential impact of changes in river nutrient supply on global ocean biogeochemistry, *Global Biogeochem. Cycles*, *21*, GB4007, doi:10.1029/2006GB002718.

Cronin, M. F., and M. J. McPhaden (2002), Barrier layer formation during westerly wind bursts, *J. Geophys. Res.*, *107*(C12), 8020, doi:10.1029/2001JC001171.

Dai, A., and K. Trenberth (2002), Estimates of freshwater discharge from continents: Latitudinal and seasonal variations, *J. Hydrometeorol.*, *3*, 660–687.

Durack, P. J., and S. E. Wijffels (2010), Fifty-year trends in global ocean salinities and their relationship to broad-scale warming, *J. Clim.*, *23*(16), 4342–4362, doi:10.1175/2010JCLI3377.1.

Ferry, N., and G. Reverdin (2004), Sea surface salinity interannual variability in the western tropical Atlantic: An ocean general circulation model study, *J. Geophys. Res.*, *109*, C05026, doi:10.1029/2003JC002122.

Ffield, A. (2005), North Brazil Current rings viewed by TRMM Microwave Imager SST and the influence of the Amazon Plume, *Deep Sea Res., Part I*, *52*(1), 137–160, doi:10.1016/j.dsr.2004.05.013.

Foltz, G. R., and M. J. McPhaden (2008), Seasonal mixed layer salinity balance of the tropical North Atlantic Ocean, *J. Geophys. Res.*, *113*, C02013, doi:10.1029/2007JC004178.

Foltz, G. R., and M. J. McPhaden (2009), Impact of barrier layer thickness on SST in the central tropical North Atlantic, *J. Clim.*, *22*(2), 285–299, doi:10.1175/2008JCLI2308.1.

Foster, R. A., A. Subramaniam, and J. P. Zehr (2009), Distribution and activity of diazotrophs in the Eastern Equatorial Atlantic, *Environ. Microbiol.*, *11*(4), 741–50, doi:10.1111/j.1462–2920.2008.01796.x.

Fratantoni, D. M., and D. A. Glickson (2002), North Brazil Current Ring generation and evolution observed with SeaWiFS, *J. Phys. Oceanogr.*, *32*, 1058–1074.

Fratantoni, D. M., and P. L. Richardson (2006), The evolution and demise of North Brazil Current rings, *J. Phys. Oceanogr.*, *36*, 1241–1264.

Garraffo, Z. D., W. E. Johns, E. P. Chassignet, and G. J. Goni (2003), North Brazil Current rings and transport of southern waters in a high resolution numerical simulation of the North Atlantic, in *Interhemispheric Water Exchange in the Atlantic Ocean, vol. 68, Elsevier Oceanogr. Ser.*, edited by G. J. Goni and P. Malanotte-Rizzoli, pp. 375–409, Elsevier, ISSN 0422-9894, ISBN 9780444512673, http://dx.doi.org/10.1016/S0422-9894(03)80155-1.

Garzoli, S. L. (1992), The Atlantic North equatorial countercurrent: Models and observations, *J. Geophys. Res.*, *97*(C11), 17,931–17,946, doi:10.1029/92JC01363.

Godfrey, J. S., and E. J. Lindstrom (1989), The heat budget of the equatorial western Pacific surface mixed layer at location studies, *J. Geophys. Res.*, *94*(C6), 8007–8017.

Goni, G. J., and W. E. Johns (2001), A census of North Brazil Current rings observed from TOPEX/POSEIDON altimetry: 1992–1998, *Geophys. Res. Lett.*, *28*(1), 1–4, doi:10.1029/2000GL011717.

Grodsky, S. A., J. A. Carton, and F. M. Bingham (2006), Low frequency variation of sea surface salinity in the tropical Atlantic, *Geophys. Res. Lett.*, *33*, L14604, doi:10.1029/2006GL026426.

Grodsky, S. A., N. Reul, G. Lagerloef, G. Reverdin, J. a. Carton, B. Chapron, Y. Quilfen, V. N. Kudryavtsev, and H.-Y. Kao (2012), Haline hurricane wake in the Amazon/Orinoco plume: AQUARIUS/SACD and SMOS observations, *Geophys. Res. Lett.*, *39*, L20603, doi:10.1029/2012GL053335.

Halliwell, G. R. (2004), Evaluation of vertical coordinate and vertical mixing algorithms in the HYbrid-Coordinate Ocean Model (HYCOM), *Ocean Modell.*, *7*(3–4), 285–322, doi:10.1016/j.ocemod.2003.10.002.

Halliwell, G. R., Jr., R. H. Weisberg, and D. A. Mayer (2003), A synthetic float analysis of upper-limb meridional overturning circulation interior ocean pathways in the tropical/subtropical Atlantic, in *Interhemispheric Water Exchange in the Atlantic Ocean*, edited by G. J. Goni and P. Malanotte-Rizzoli, pp. 93–136, Elsevier, Amsterdam.

Hansen, D., and P.-M. Poulain (1996), Quality control and interpolations of WOCE-TOGA drifter data, *J. Atmos. Oceanic Technol.*, *13*, 900–909.

Hellweger, F. L., and A. L. Gordon (2002), Tracing Amazon River water into the Caribbean Sea, *J. Mar. Res.*, *60*(4), 537–549, doi:10.1357/002224002762324202.

Hu, C., E. T. Montgomery, R. W. Schmitt, and F. E. Müller-Karger (2004), The dispersal of the Amazon and Orinoco River water in the tropical Atlantic and Caribbean Sea: Observation from space and S-PALACE floats, *Deep Sea Res., Part II*, *51*(10–11), 1151–1171, doi:10.1016/j.dsr2.2004.04.001.

Johns, W., T. N. Lee, F. A. Schott, R. J. Zantopp, and R. H. Evans (1990), The North Brazil Current retroflection: Seasonal structure and eddy variability, *J. Geophys. Res.*, *95*(C12), 22,103–22,120.

Josey, S. A., E. C. Kent, and P. K. Taylon (1999), New insights into the ocean heat budget closure problem from analysis of the SOC air–sea flux climatology, *J. Clim.*, *12*(9), 2856–2880, doi:10.1175/1520-0442(1999)012.

Kara, A. B., A. J. Wallcraft, H. E. Hurlburt, and W.-Y. Loh (2009), Quantifying SST errors from an OGCM in relation to atmospheric forcing variables, *Ocean Modell.*, *29*(1), 43–57, doi:10.1016/j.ocemod.2009.03.001.

Large, W. G., J. C. McWilliams, and S. C. Doney (1994), Oceanic vertical mixing: A review and a model with a nonlocal boundary layer parameterization, *Rev. Geophys.*, *32*(4), 363–403, doi:10.1029/94RG01872.

Lentz, S. J. (1995), Seasonal variations in the horizontal structure of the Amazon Plume inferred from historical hydrographic data, *J. Geophys. Res.*, *100*, 2391–2400.

Lentz, S. J., and R. Limeburner (1995), The Amazon River Plume during AMASSEDS: Subtidal current variability and the importance of wind forcing, *J. Geophys. Res.*, *100*(C2), 2355–2375, doi:10.1029/94JC01411.

Locarnini, R. A., A. V. Mishonov, J. I. Antonov, T. P. Boyer, H. E. Garcia, O. K. Baranova, M. M. Zweng, and D. R. Johnson (2010), *World Ocean Atlas 2009, Volume 1: Temperature*, edited by S. Levitus, p. 184, U.S. Gov. Print. Off., Washington, D. C.

Lukas, R., and E. J. Lindstrom (1991), The mixed layer of the western equatorial Pacific Ocean, *J. Geophys. Res.*, *96*, 3343–3358.

Lumpkin, R., and S. L. Garzoli (2005), Near-surface circulation in the Tropical Atlantic Ocean, *Deep Sea Res., Part I*, *52*(3), 495–518, doi:10.1016/j.dsr.2004.09.001.

Marengo, J. A., J. Tomasella, W. R. Soares, L. M. Alves, and C. A. Nobre (2011), Extreme climatic events in the Amazon basin, *Theor. Appl. Climatol.*, *107*(1–2), 73–85, doi:10.1007/s00704-011-0465-1.

Masson, S., and P. Delecluse (2001), Influence of the Amazon River runoff on the tropical Atlantic, *Phys. Chem. Earth, Part B*, *26*(2), 137–142.

Müller-Karger, F. E., C. R. McClain, and P. L. Richardson (1988), The dispersal of the Amazon's water, *Nature*, *333*(6168), 56–59, doi:10.1038/333056a0.

Müller-Karger, F. E., C. R. McClain, T. R. Fisher, W. E. Esaias, and R. Varela (1989), Pigment distribution in the Caribbean sea: Observations from space, *Prog. Oceanogr.*, *23*(1), 23–64, doi:10.1016/0079-6611(89)90024-4.

Müller-Karger, F. E., P. L. Richardson, and D. J. McGillicuddy (1995), On the offshore dispersal of the Amazon's Plume in the North Atlantic: Comments on the paper by A. Longhurst, "Seasonal cooling and blooming in tropical oceans," *Deep Sea Res., Part I*, *42*(11–12), 2127–2137, doi:10.1016/0967-0637(95)00085-2.

Nikiema, O., J.-L. Devenon, and M. Baklouti (2007), Numerical modeling of the Amazon River plume, *Cont. Shelf Res.*, *27*(7), 873–899, doi:10.1016/j.csr.2006.12.004.

Nittrouer, C. A., and D. J. DeMaster (1986), Sedimentary processes on the Amazon continental shelf: Past, present and future research, *Cont. Shelf Res.*, *6*(1–2), 5–30, doi:10.1016/0278-4343(86)90051-8.

Pailler, K., B. Bourlès, and Y. Gouriou (1999), The barrier layer in the western tropical Atlantic Ocean, *Geophys. Res. Lett.*, *26*(14), 2069, doi:10.1029/1999GL900492.

Philander, S. G. H., and R. C. Pacanowski (1986), A model of the seasonal cycle in the tropical Atlantic Ocean, *J. Geophys. Res.*, *91*(C12), 14,192–14,206, doi:10.1029/JC091iC12p14192.

Poje, A. C., A. C. Haza, T. M. Özgökmen, M. G. Magaldi, and Z. D. Garraffo (2010), Resolution dependent relative dispersion statistics in a hierarchy of ocean models, *Ocean Modell.*, *31*(1–2), 36–50, doi:10.1016/j.ocemod.2009.09.002.

Richardson, P. L., and T. K. McKee (1984), Average seasonal variation of the Atlantic Equatorial Currents from historical ship drifts, *J. Phys. Oceanogr.*, *14*(7), 1226–1238.

Richardson, P. L., and G. Reverdin (1987), Seasonal cycle of velocity in the Atlantic North Equatorial Countercurrent as measured by surface drifters, current meters, and ship drifts, *J. Geophys. Res.*, *92*(C4), 3691–3708, doi:10.1029/JC092iC04p03691.

Roemmich, D., and M. Morris (1994), Fresh equatorial jets, *J. Phys. Oceanogr.*, *24*, 540–558.

Salisbury, J., D. Vandemark, J. Campbell, C. Hunt, D. Wisser, N. Reul, and B. Chapron (2011), Spatial and temporal coherence between Amazon River discharge, salinity, and light absorption by colored organic carbon in western tropical Atlantic surface waters, *J. Geophys. Res.*, *116*, C00H02, doi:10.1029/2011JC006989.

Schiller, R. V., and V. H. Kourafalou (2010), Modeling river plume dynamics with the HYbrid Coordinate Ocean Model, *Ocean Modell.*, *33*(1–2), 101–117, doi:10.1016/j.ocemod.2009.12.005.

Schott, F. A., and C. W. Böning (1991), The WOCE model in the western equatorial Atlantic: Upper layer circulation, *J. Geophys. Res.*, *96*(C4), 6993–7004, doi:10.1029/90JC02683.

Servain, J., A. Busalacchi, A. Moura, M. McPhaden, G. Reverdin, M. Vianna, and S. Zebiak (1998), A pilot research moored array in the tropical Atlantic "PIRATA," *Bull. Am. Meteorol. Soc.*, *79*, 2019–2031.

Stukel, M. R. R., V. J. Coles, M. T. Brooks, and R. R. Hood (2013), Diatom-diazotroph assemblage growth in the Amazon River Plume: Top-down, bottom-up and physical controls, *Biogeochemistry*, *10*(8), 13,931–13,976, doi:10.5194/bgd-10-13931-2013.

Subramaniam, A., et al. (2008), Amazon River enhances diazotrophy and carbon sequestration in the tropical North Atlantic Ocean, *Proc. Natl. Acad. Sci. U.S.A.*, *105*(30), 10,460–10,465.

Uppala, S. M., et al. (2005), The ERA-40 re-analysis, *Q. J. R. Meteorol. Soc.*, *131*(612), 2961–3012, doi:10.1256/qj.04.176.

Urbano, D. F., M. Jochum, and I. C. A. da Silveira (2006), Rediscovering the second core of the Atlantic NECC, *Ocean Modell.*, *12*, 1–15.

Vizy, E. K., and K. H. Cook (2010), Influence of the Amazon/Orinoco Plume on the summertime Atlantic climate, *J. Geophys. Res.*, *115*, D21112, doi:10.1029/2010JD014049.

Vorosmarty, C. J., B. M. Fekete, and B. A. Tucker (1998), Global River Discharge, 1807–1991, V. 1.1 (RivDIS), data set, Oak Ridge National Laboratory Distributed Active Archive Center, Oak Ridge, Tenn., doi:10.3334/ORNLDAAC/199. [Available at http://www.daac.ornl.gov.]

Wilson, W. D., E. Johns, and R. L. Molinari (1994), Upper layer circulation in the western tropical North Atlantic Ocean during August 1989, *J. Geophys. Res.*, *99*(C11), 22,513–22,523, doi:10.1029/94JC02066.

Xie and Arkin (1997), Global Precipitation: A 17-year monthly analysis based on gauge observations, satellite estimates, and numerical model outputs, *Bulletin of the American Meteorological Society*, *78*, 2539–2558.